Modelling the riverine δ7Li variability throughout the Amazon Basin

Pierre Maffre, Yves Goddéris, Nathalie Vigier, Jean-Sébastien Moquet, Sébastien Carretier

Modelling the riverine δ^7Li variability throughout the Amazon Basin

Pierre Maffre[1], Yves Goddéris[1*], Nathalie Vigier[2], Jean-Sébastien Moquet[3], Sébastien Carretier[1]

[1] Géosciences Environnement Toulouse, CNRS – Université Paul Sabatier – IRD, Toulouse, France
[2] Laboratoire d'Océanographie de Villefranche, CNRS – Université Pierre et Marie Curie, Sorbonne Université, Villefranche-sur-Mer, France
[3] Institut de Physique du Globe de Paris, France

[*] Corresponding author: yves.godderis@get.omp.eu

Keywords
Lithium isotopes, weathering, Amazon, model

Abstract

The present study investigates the processes controlling the elementary and isotopic cycle of the lithium over the Amazon basin. A numerical model is developed to simulate two major processes that have been proposed as key controls of the river lithium isotopic composition: weathering reactions inside the regolith, accounting for secondary phase formation, and interactions between riverine water and secondary phases in floodplain. Both processes generate fractionation of lithium isotopes ("batch" fractionation and "Rayleigh" distillation respectively) that potentially control the riverine isotopic composition of the Amazon and its tributaries.

A study of the model parameters shows that two different regimes are impacting the lithium isotopic composition of the rivers within the Amazon catchment. In the South (Madeira and its tributaries), the lithium isotopic signature of river waters can be explained by lithium release and fractionation during weathering reactions in the regolith, followed by "Rayleigh distillation" in the floodplain increasing progressively the lithium isotopic composition, in agreement with a previously published hypothesis. In contrast, the lithium isotopic composition of rivers located in the northern part of the Amazon watershed (Solimoes and tributaries) cannot be simulated by the model assuming the same processes than in the southern part. Model optimization suggests than the nature of the material being eroded and weathered is important. In the North, fresh source rocks of volcanic origin releases large amount of Li and promotes rapid smectite precipitation, allowing the riverine δ^7Li to rise before flowing through floodplains. This result suggests that the environments able to generate high riverine δ^7Li (higher than 25‰) are complex and not firmly identified yet.

1. Introduction

The lithium isotopic composition (δ^7Li) of river waters is a potential tracer of continental weathering processes (e.g. Huh et al., 1998; Vigier et al., 2009; Millot et al., 2010b; Dellinger et al., 2014, 2015; Pogge von Strandmann et al., 2017). Indeed, the isotopic composition of dissolved riverine lithium is the result of complex interactions between solids and the water flowing through the Critical Zone. The dissolution of primary minerals releases lithium in solution without significant isotopic fractionation (Pistiner and Henderson, 2003; Wimpenny et al., 2010a; Verney-Carron et al., 2011). Precipitation of secondary clay minerals retains about 80 to 90% of the lithium released by rock and mineral leaching, and this incorporation occurs with a strong isotopic fractionation ranging from 10‰ to 25‰ at low temperature (e.g. Pistiner and Henderson, 2003; Vigier et al., 2008; Millot et al., 2010a; Dupuis et al., 2017), in favor of the light –^{6}Li– isotope. As a result, river dissolved phases are systematically enriched in ^{7}Li in small and large watersheds (e.g. Kısakűrek et al., 2005; Huh et al., 1998; Dellinger et al., 2014; Pogge von Strandmann et al., 2017).

A consensus, based on both observational and modelling studies (Stallard and Edmond, 1983; Riebe et al., 2004; West et al., 2005; Gabet and Mudd, 2009; West, 2012), emerged for defining two major weathering poles: some areas are characterized by a “weathering-limited” regime where primary minerals are not completely weathered before being eroded away. In those regions, dissolution rates of fresh minerals are the limiting process. The export of dissolved species is relatively fast, soil residence time is small and secondary clay formation remains limited. Generally, tectonically-active mountain ranges belong to this pole (e.g. West et al., 2005). If the corresponding soil thickness is small, the lithium isotopic composition of the runoff (superficial waters) is expected to be maintained at a low value, close to the continental source rocks (Dellinger et al., 2015; Bouchez et al., 2013; Pogge von Strandmann and Henderson, 2015). Other areas, mostly located in the plains, lowlands or cratons, are characterized by the supply-limited regime where residence time of minerals within the regolith is long enough to completely remove primary phases at the surface. In these regions, the time of water-rock interactions is longer and secondary phase formation is facilitated. Thus, in these flat regions, removal of dissolved Li by secondary mineral formation is expected to increase the runoff δ^7Li values.

Given the isotopic composition of the continental rocks (1.7‰ on average, Teng et al., 2009) and accounting for the known values of lithium isotopic fractionations (around 20‰), the maximum δ^7Li value that river waters can reach (assuming an equilibrium process) is close to 22‰. However, a non negligible amount of rivers display much higher δ^7Li values, reaching 30 to 40% (Huh et al., 1998, 2001; Kısakűrek et al., 2005; Vigier et al., 2009; Millot et al., 2010b; Wimpenny et al., 2010b). For large basins, it has been hypothesized that the

high values reached in low relief area and in floodplains could be the result of a continuous isotopic fractionation similar to a Rayleigh distillation (Vigier et al., 2009; Bagard et al., 2015; Dellinger et al., 2015; Pogge von Strandmann et al., 2017). In floodplains, the dissolved lithium released upstream continuously interacts with secondary mineral phases, reducing the dissolved lithium load while enriching it in ^{7}Li. Thus, the elevated $\delta^{7}Li$ values of the downstream tributaries of the Madeira and Solimões rivers (Amazon Basin, Dellinger et al., 2015) can be explained by Rayleigh distillation law, based on correlations between the river isotopic ratio and its dissolved Li concentration. However, in the specific case of the Solimoes high $\delta^{7}Li$ values are also observed close to the outlet of the Andes, potentially suggesting the existence of enrichment in ^{7}Li before the water flows through floodplains. High values for mountain rivers have been compiled by Schmitt et al. (2012). Conversely more recent contributions have reported low $\delta^{7}Li$ values in mountaineous rivers (Millot et al., 2010; Pogge von Strnadmann et al., 2017). These contradictory results do not allow drawing a general picture, and suggest the existence of a variety of processes impacting the riverine $\delta^{7}Li$ that are not fully understood yet.

In the present contribution, we build a comprehensive numerical model simulating the lithium elemental and isotopic behaviour at the continental scale. The model accounts for both secondary mineral precipitation in regolith and for continuous interactions between river water and secondary phases in floodplains. As a test for the ability of these two processes to explain the first order pattern of the riverine $\delta^{7}Li$, we simulate the elemental and isotopic mass balance over the Amazon. The Amazon contributes significantly to the global dissolved and suspended fluxes delivered to the oceans. It includes both “supply limited” and “weathering limited” domains and extended areas of permanent or seasonal floodplains. These characteristics make the Amazon catchment an ideal laboratory to simulate the processes impacting the riverine lithium dissolved load and its isotopic composition. The Amazon watershed is monitored by the HYBAM observatory providing high-frequency measurements of water discharge, suspended and dissolved load at 40 stations distributed within the catchment (see Fig. 1, and Appendix A). Erosion and weathering fluxes are known at the geomorphologic domains scale (Moquet et al., 2011, 2016). Moreover, the lithium isotopic composition and elemental concentrations are available at various measurement sites (Dellinger et al., 2015).

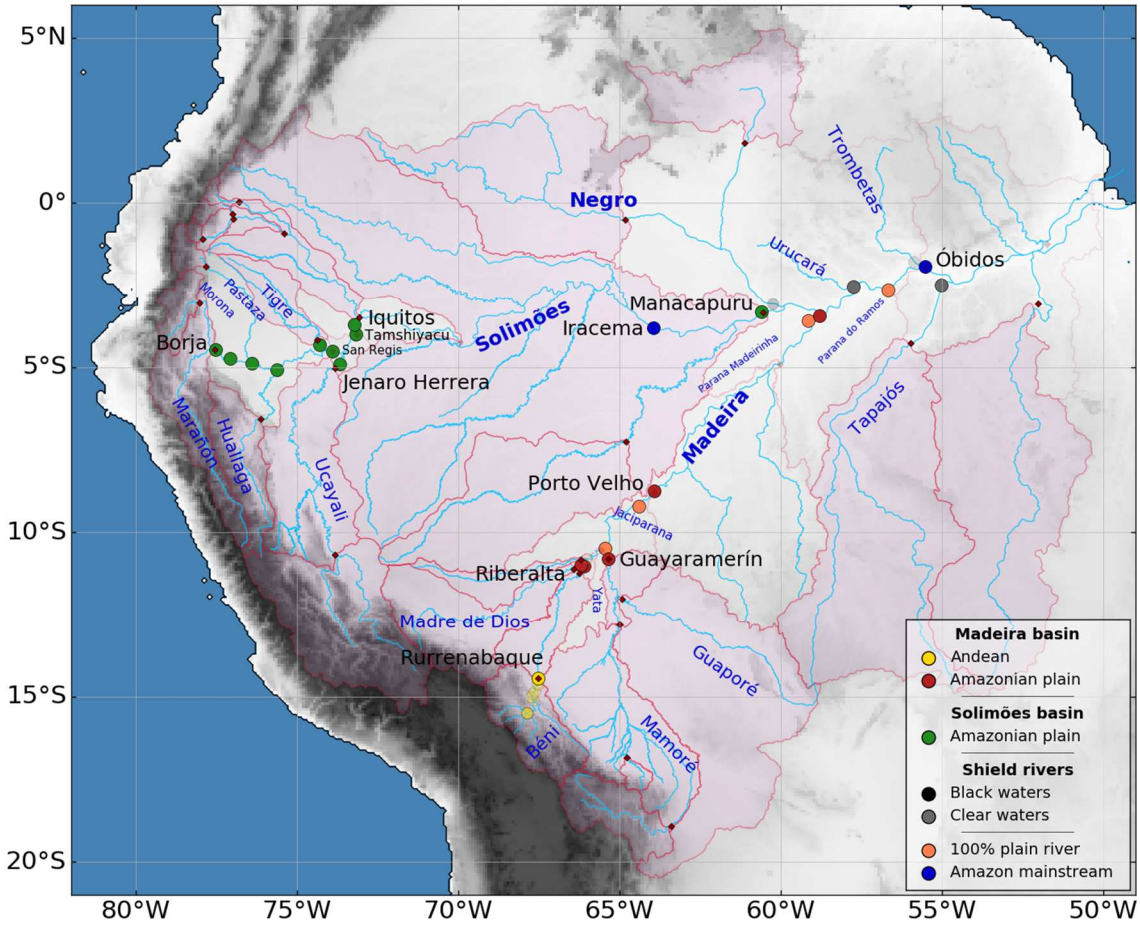

Figure 1: Map of the Amazon tributaries (blue lines) showing the monitoring stations where riverine δ^7Li has been measured (Dellinger et al., 2015) (colored circles), the HYBAM monitoring stations (dark grey diamonds) and corresponding watersheds (light red shades).

2. River water δ^7Li in the Amazon Basin

Dellinger et al. (2015) published a detailed database for the Amazon watershed, gathering 39 sample sites, from the Andes to the outlet in the Atlantic Ocean. Measured Li isotopic composition of river waters range from 2‰ to 33‰ and can be explained by considering three types of waters contributing to the Amazon main flow: the white, clear, and black waters. “Black” waters are characterized by high organic matter content and low δ^7Li (2‰ to 10‰), close to the bedrock values. Dellinger et al. (2015) suggest that the high organic acid content of the black waters promotes a complete dissolution of the secondary phases. This weathering congruency drives the δ^7Li of the black waters close to the continental bedrock

values, explaining the low riverine δ^7Li. This process was also evidenced for some rivers draining the Congo basin (Henchiri et al., 2016). The “white” waters are characteristic of the Andes and floodplains, with highly variable δ^7Li (from 4 to 33‰). White waters contribute for more than 70% of the dissolved lithium released to the ocean by the Amazon River. Finally, the last water pool is flowing on the Amazonian shield (clear waters) and contributes for less than 10% to the dissolved lithium flux of the Amazon river. Based on their measurements, Dellinger et al. (2015) do not observe a significant seasonality in the δ^7Li, except for the Négro and Madeira rivers, with maximum differences about 9.2‰ and 6.5‰ respectively.

In the present contribution, we only focus on the white and clear waters. Modelling organic matter content and dissolution by organic acid is beyond the capacity of this study. In white and clear waters, δ^7Li below about 20‰ have been explained by Dellinger et al. (2015) by an equilibrium fractionation occurring inside the weathering profiles. Primary mineral dissolution releases Li with a low isotopic signature, and the subsequent formation of secondary minerals increases the δ^7Li of the circulating water. Higher values plots along a Rayleigh distillation line, leading these authors to postulate that continuous interactions between water and secondary minerals occur in flood plains and allow the water δ^7Li to rise above the limit of the equilibrium fractionation.

The objective is to calculate the isotopic composition of the waters draining the Amazon watershed. Given that the two processes suspected to control the Amazon Li isotopic signature are geographically distributed over the watershed, it is mandatory to build a spatially resolved model. The simulated values are then compared to the available data at various locations over the watershed.

3. Model description

3.1. Overall design of the model

We built a spatially resolved numerical model of the Li elemental and isotopic behaviour over the Amazon watershed. The model is designed as a tool to test the “floodplain” hypothesis. It requires the knowledge of the erosion and weathering fluxes. Both are calculated using published models (Gabet and Mudd, 2009; West, 2012; Maffre et al., 2018) and a corrective factor is applied to match the spatially-distributed data. Those fluxes are then injected into a numerical model simulating (1) the lithium isotopic and elemental behaviour inside the

regoliths (vertical 1D model, referred in the text as the "regolith component"), (2) and the impact of lateral floodings on the Li terrestrial cycle. (1D ramified model referred as "floodplain component"). As described below, each grid cell is divided into a floodplain fraction where lateral movements of water modify the elemental and isotopic composition of dissolved lithium. The remaining part of the grid cell is assumed to behave as a regolith, which controls the Li composition of the draining waters. Then both components are mixed.

3.2. Modeling Li isotopes in weathering profiles: the regolith component

The backbone of the regolith component consists of a set of 4 equations (Eq. 1 to Eq. 4). The specific release of Li by primary mineral dissolution $F_{diss(Li)}$ (mol/m^2/yr) on each grid element (0.5°lat x 0.5°long) of the Amazon watershed is set proportional to the main cation release, itself calculated according to the steady state weathering model of West (2012):

$$F_{diss}(\mathrm{cat}) = \chi_{\mathrm{cat}} \cdot E \cdot \left\{1 - \exp\left[-K \cdot \exp\left(-\frac{E_A}{R}\left(\frac{1}{T} - \frac{1}{T_0}\right)\right) \cdot \left(1 - e^{-k_w q}\right) \cdot \frac{(h/E)^{\sigma+1}}{\sigma+1}\right]\right\} \quad (1)$$

χ_{cat} is the abundance of cations in rocks (in mol/m^3), E_A is here the activation energy for rock dissolution and K, k_w and σ three parameters (see Table 1). h is the local regolith thickness and E the physical removal of material by erosion. Both are spatially distributed over the watershed, E comes from the reconstruction of Ludwig and Probst (1998). We assume a constant lithium/cation ratio of source rocks ($\chi_{\mathrm{Li}}/\chi_{cat}$) equals to 1.2x10^{-4} (Teng et al., 2009).

$F_{sp}^{reg}(\mathrm{Li})$ is the specific uptake of Lithium by secondary mineral phases within the regolith (mol/m^2/yr). We assume that the ratio $F_{sp}^{reg}(\mathrm{Li})/F_{diss}(\mathrm{Li})$ depends on the residence time of the water inside the regolith, written as $\varphi h/q$, where q is the vertical water drainage (precipitation minus evapotranspiration, m yr^{-1}), h the regolith thickness (m) and φ the regolith porosity. (m^3/m^3). To describe mathematically the dependence of $F_{sp}^{reg}(\mathrm{Li})/F_{diss}(\mathrm{Li})$ on the water residence time, we choose a Michaelis function, so that $F_{sp}^{reg}(\mathrm{Li})/F_{diss}(\mathrm{Li})$ is equal to zero for a null water residence time and to 1 (all lithium is retained in secondary phases) for infinite water residence time:

$$F_{sp}^{reg}(\mathrm{Li}) = \frac{1}{1+\frac{\tau_o}{\varphi h/q}} F_{diss}(\mathrm{Li}) \quad (2)$$

The regolith thickness *h* is calculated using the Gabet and Mudd (2009) model describing the evolution of a regolith under the combined effect of regolith production and erosion. According to this model, the regolith production decreases exponentially with the regolith thickness. Following Carretier et al. (2014), we made the equation for regolith production rate dependent on temperature and runoff. For each grid cell, the steady state thickness *h* of the regolith can be calculated according to:

$$h = h_o \cdot \ln\left(k_{rp} \cdot q \cdot \exp\left(-\frac{E_A^{rp}}{R}\left(\frac{1}{T} - \frac{1}{T_0}\right)\right) / E \right) \quad (3)$$

where h_o is the decay depth and k_{rp} is the soil production constant, T is the mean annual temperature, q is the water drainage, E_A^{rp} the apparent activation energy for the regolith production, R the ideal gas constant and k_{rp} a scaling constant (see Table 1).

The specific flux of lithium leaving the regolith and reaching the hydrographic network $F_{leach}(\mathrm{Li})$ (mol/m^2/yr) is the difference between the specific flux of Li released by primary mineral dissolution and the specific flux of Li retained by secondary phases.

$$F_{leach}(\mathrm{Li}) = F_{diss}(\mathrm{Li}) - F_{sp}^{reg}(\mathrm{Li}) \quad (4)$$

The system of equations 1 to 4 defines $F_{sp}^{reg}(\mathrm{Li})$, $F_{diss}(\mathrm{Li})$, $F_{leach}(\mathrm{Li})$ and *h*, for each grid cell of the Amazon watershed.

Practically, the model is fed with the output of two published models giving the spatial distribution of the weathering flux F_{diss} (main cations) and of the physical erosion *E* (respectively West, 2012; Ludwig and Probst, 1998). To limit the propagation of the uncertainties brought by these models into the lithium model, we applied corrective factors to the calculation of F_{diss} and *E*. Over each monitored sub-basin of the Amazon, we use the HYBAM database to correct the calculated fields of erosion and cation release by silicate dissolution. The weathering and erosion are multiplied by a corrective factor, so that they fit the measured values at the outlet of the sub-basin, once integrated over the sub-basin. The erosion and weathering fields shown on Fig. 2 (a and b respectively) are the corrected ones. The details of this correction procedure can be found in Appendix A.

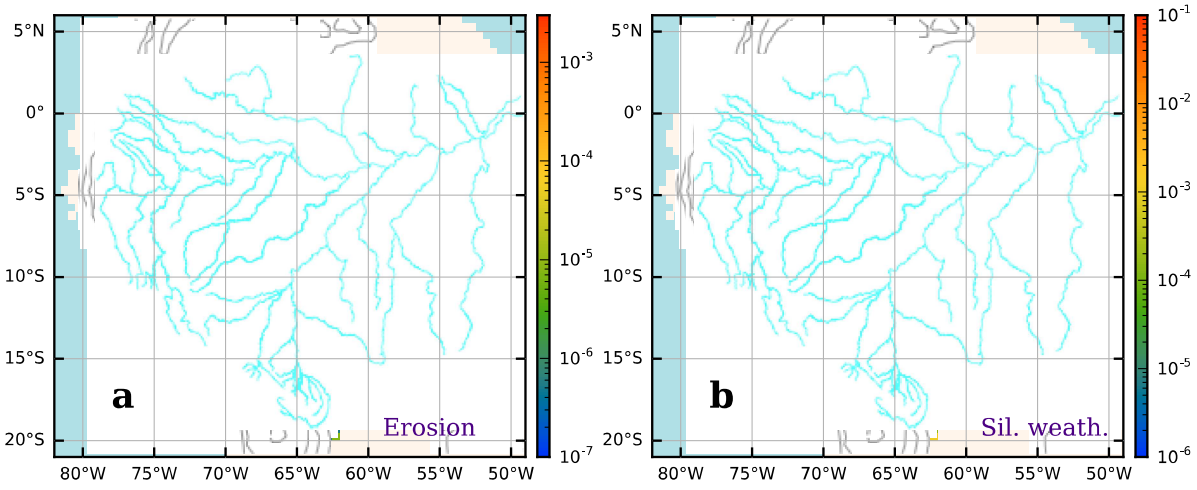

Figure 2: (a) Erosion rates (m/y) and (b) silicate weathering rates (major cation flux in kg/m^2/y) over the Amazonian basin. The erosion field is taken from Ludwig and Probst (1998), the weathering field is computed with Eq. 1. Both are corrected with HYBAM data (see section 3.4 and Appendix A). The grey areas correspond to locations where the erosion or weathering rates are equal to zero. Weathering rate goes down to zero when the erosion does, or because the regolith thickness falls down to zero. Blue lines show the main rivers; the white arrows show water routing in the model grid; black contours are elevation isolines (500m, 1000m, 2000m, 4000m and 6000m).

Regarding isotopes, lithium is assumed to follow an equilibrium fractionation occurring during the precipitation of secondary phases, primary phases being congruently dissolved (Bouchez et al., 2013; Dellinger et al., 2015). The isotopic mass balance is written as:

$$\delta^7_{riv}\mathrm{Li} = \delta^7_{rock}\mathrm{Li} + \frac{F^{reg}_{sp}(\mathrm{Li})}{F_{diss}(\mathrm{Li})}\Delta_{land} \quad (5)$$

δ^7_{riv}Li is the δ^{7}Li value of waters leaving the regolith, δ^7_{rock}Li is the δ^{7}Li value of the source rocks (1.7‰, Teng et al., 2004, 2009), and Δ_{land} the corresponding isotope fractionation factor during the incorporation of dissolved Li into secondary phases. This fractionation factor is mainly controlled by temperature (Vigier et al., 2008) and, to a lesser extent, by chemistry (Li and West, 2014; Dupuis et al., 2017). Here the fractionation factor is made dependent on temperature through a T^{-2} fit (T being the temperature, in K) supported by both experimental measurements and ab-initio computation at various temperatures (Dupuis et al., 2017).

$$\Delta_{land} = \frac{1.63\cdot10^6}{T^2} - 2.04 \quad (6)$$

The calculated value of Δ_{land} is equal to 17‰ at 20°C, a value consistent with Dellinger et al. (2015) observations and with laboratory experiments (Hindshaw et al, 2019). In the model, it decreases to 16‰ in the warmest places and increases to 19‰ in the coldest. (Fig. 3).

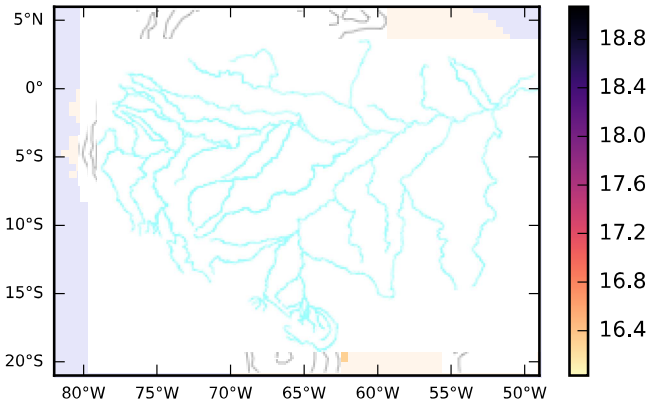

Figure 3: Li isotopic fractionation occurring during the precipitation of secondary phases Δ_{land} over the Amazon catchment (‰) as computed by Eq. 6.

3.3. Modelling Li isotopes in floodplains: the floodplain component

The vertical "regolith" component is coupled to the second component: an horizontal ramified 1-D reactive transport model that simulates the Li isotopic and elemental budgets of the main rivers of the Amazon catchment, assumed at steady-state (all time derivatives are set to zero). This model component is designed to calculate the impact of lateral flooding. If x is the river coordinate (increasing from head to mouth) and $F_{riv}(\mathrm{Li})(x)$ is the flux of lithium carried by the river at coordinate x (in mol/yr), the elementary mass budget can be written as:

$$\frac{dF_{riv}(\mathrm{Li})}{dx} = w\left(F_{diss}(\mathrm{Li}) - F_{sp}^{flood}(\mathrm{Li})\right) \quad (7)$$

where w is the river width, and $F_{diss}(\mathrm{Li})$ and $F_{sp}^{flood}(\mathrm{Li})$ are respectively the specific dissolved and retention lithium fluxes (in mol/m^2/y) within floodplains. As river water enters in contact with sediments containing primary minerals, we calculate the supply of Li by mineral dissolution using the same methodology than the one used for the regolith component (which is applied to the fraction of the grid cell not flooded). Conversely, the retention of lithium by

293 secondary phases is now written F_{sp}^{flood}, to distinguish it from F_{sp}^{reg}. The reason for this is that
294 F_{sp}^{flood} might be a different process than the precipitation of secondary minerals, or that it can
295 be limited by other factors than the production term $F_{diss}(\mathrm{Li})$. To our knowledge, no study has
296 proposed a mathematical relation to quantify it. The incorporation of lithium on clays (or other
297 secondary minerals, such as aluminium hydroxides) is still poorly understood. It is yet
298 unclear whether riverine water can exchange lithium with clays already formed or lithium can
299 only be integrated in clays at the time they precipitate. In the absence of such information,
300 we tested the two possibilities, assuming basic mathematical equations. In the first case, the
301 Li riverine concentration is the only control:
302
303 $$F_{sp}^{flood}(\mathrm{Li}) = k_{sp}[\mathrm{Li}]_{riv}{}^{a} \quad (8)$$
304
305 Where k_{sp} and the exponent a are two adjustable parameters. They can be seen
306 respectively as the kinetic constant and the order of the reaction. Eq. (8) will be referred in
307 the following as the case #1, and can be interpreted as a case where secondary phases are
308 pre-existing in the sediment and that Li is removed by adsorption or any similar process,
309 limited by the available amount of lithium supplied by the rivers.
310
311 In the second case, F_{sp}^{flood} is supposed to be limited by the local rate of secondary phases
312 precipitation, this last being proportional to the local rate of primary mineral dissolution. But
313 the difference with the vertical “regolith” component is that, even if the removal of lithium in
314 the flooded part of the grid cell is controlled by the precipitation of secondary minerals, it
315 must exceed the supply of lithium by the local primary mineral dissolution to allow the
316 dissolved riverine δ^7Li to increase. This is made possible by the supply of dissolved lithium
317 from upstream flows. Mathematically speaking, the maximal value for F_{sp}^{flood} is set equal to
318 $K_m F_{diss}(\mathrm{Li})$ where K_m is the lithium storing capacity of secondary phases with respect to
319 primary phases. In other words, if 1 mole of primary minerals contains 1 mole of Li, the
320 secondary minerals formed from that minerals could contain at most K_m mole of Li. K_m has
321 to be greater than 1 to make possible a net uptake of lithium in floodplain at position x from
322 the river head. In addition, we supposed a kinetic limitation at low lithium concentrations.
323 With again a Michaelis-like relation, these conditions can be written as follows:
324
325 $$F_{sp}^{flood}(\mathrm{Li}) = \frac{K_m F_{diss}(\mathrm{Li})}{1 + \frac{K_m F_{diss}(\mathrm{Li})}{k_{sp}[\mathrm{Li}]_{riv}}} \quad (9)$$
326

k_{sp} is here the kinetic constant. Eq. (9) will be referred as the case #2. The theoretical behaviour of the floodplain model is explored in Appendix B.

Given the local fractionation rule ($\delta^7_{sp}\mathrm{Li(x)} = \delta^7_{riv}\mathrm{Li}(x) - \Delta_{land}$), the isotopic budget of the local riverine δ⁷Li becomes:

$$F_{riv}(\mathrm{Li})\frac{d\delta^7_{riv}\mathrm{Li}}{dx} = w\,F_{diss}(\mathrm{Li})\left(\delta^7_{rock}\mathrm{Li} - \delta^7_{riv}\mathrm{Li}\right) + wF^{flood}_{sp}(\mathrm{Li})\Delta_{land} \quad (10)$$

where $\delta^7_{riv}\mathrm{Li}$ is the δ⁷Li value of riverine water at the distance x from the head of the river, $\delta^7_{sp}\mathrm{Li}$ the δ⁷Li of locally formed secondary phases and $\delta^7_{rock}\mathrm{Li}$ is the isotopic ratio of the source rocks. *w* is the width of the flooded area connected to the river at the distance *x* from the river head. It can be interpreted as the characteristic distance reached laterally by floods. We assume that riverine water and overbank water are instantaneously mixed, so the system behaves like a homogenous channel of width w. Yet, w varies along the river course, according to the lateral extension of the flood plains.

The complete ramified model is built accounting for the hydrographic network. The whole river basin is discretized on a latitude-longitude mesh (the resolution is 0.5°x0.5°). Each cell of the mesh is connected to a unique downstream cell according to the hydrographic network. If L is the length of the river course within a single cell, Eq. 7 and 10 are integrated between *0* (where the river enters the cell) and L (where the river leaves the cell).

3.4. Coupling *regolith* and *floodplain* components

The cells of the model spatial grid are sorted from upstream to downstream. Then the integration of the two model components is performed cell by cell according to the following steps:

1) Running the *regolith* model component (Eq. 2 and 5) and compute $F_{riv}(\mathrm{Li})\langle hillslope\rangle$ and $\delta^7_{riv}\mathrm{Li}\langle hillslope\rangle$
2) Averaging the outputs of all upstream cells ($F_{riv}(\mathrm{Li})$ and $\delta^7_{riv}\mathrm{Li}$) to initialize *the plain* model
3) Integrating the *floodplain* model (Eq. 7 and 10) from $x = 0$ to $x = L$ and compute $F_{riv}(\mathrm{Li})\langle floodplain\rangle$ and $\delta^7_{riv}\mathrm{Li}\langle floodplain\rangle$
4) Weighting the *weathering* and *plain* outputs by the ratio unflooded or flooded surfaces to the total grid cell surface, to compute the values of $F_{riv}(\mathrm{Li})$ and $\delta^7_{riv}\mathrm{Li}$ leaving the cell

These steps are illustrated in Fig. 4. The numerical solving of the coupled model is detailed in Appendix C.

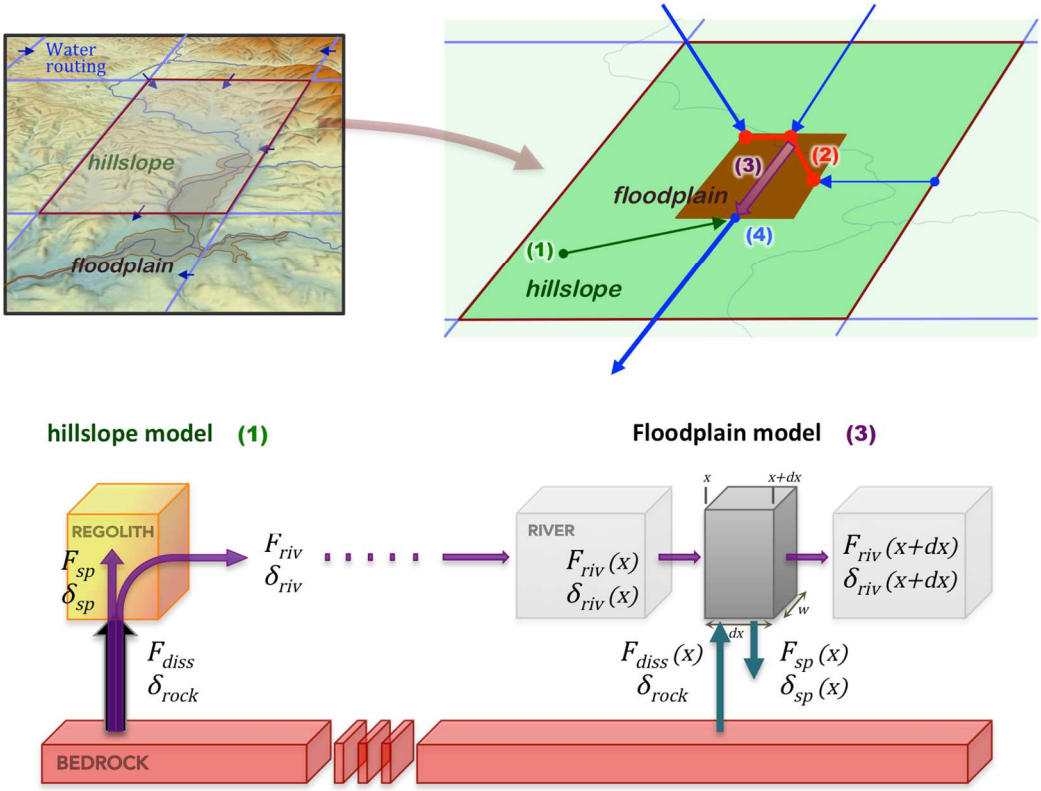

Figure 4: Schematic representation of the *hillslope* lithium model, *floodplain* model and their coupling. Cells are connected by the hydrographic network (blue arrows). The upper-right scheme summarizes the four steps of the model coupling: 1) running the *hillslope* model; 2) initializing the *floodplain* model; 3) integrating the *floodplain* model; 4) mixing (see section 3.3). The lower scheme is a simplified 1D representation of the *hillslope* and *floodplain* models. It illustrates the mass and isotopic budget of the *hillslope* box model and of an infinitesimal slice (between *x* and *x+dx*) of the *floodplain* model.

3.5. Boundary conditions and parameterizations.

The model parameters are listed in Table 1 and the main variables in Table 2 (next two pages).

384

Table 1: List of model parameters.

Parameter	Description	Units	Value	Reference
h_o	Characteristic depth of regolith production exponential decay	m	2.73	Best fit in Maffre et al. (2018)
k_{rp}	Scaling constant of regolith production	-	2e-3	Adapted from Maffre et al. (2018)'s best fit
E_A^{rp}	Activation energy at $T_o = 25°C$ for regolith production	J/K/mol	48200	Oliva et al. (2003)
E_A	Activation energy at $T_o = 25°C$ for mineral dissolution	J/K/mol	1000	Best fit in Maffre et al. (2018)
k_w	Runoff sensitivity constant of mineral dissolution	$m^{-1}yr$	0.076	West (2012)
σ	Time-dependence exponent of mineral dissolution	-	-0.1	West (2012)
K	Scaling constant of mineral dissolution	-	5e-4	Best fit in Maffre et al. (2018)
χ_{cat}	Main cation abundance in unweathered bedrock	mol/m^3	4750	Best fit in Maffre et al. (2018)
$\chi_{\mathrm{Li}}/\chi_{\mathrm{cat}}$	Li abundance with respect to main cations in bedrock	-	$1.2x10^{-4}$	Teng et al. (2009)
$\delta^7_{rock}\mathrm{Li}$	Li isotopic ratio of bedrock	‰	1.7	Teng et al. (2004; 2009)
φ	Regolith porosity	-	0.2	Arbitrary (see current section)
τ_o	Li half-retention residence time in regolith	yr	0.8	calibrated
k_{sp}	Scaling constant for Li retention in floodplain	-		explored
a	Exponent of Li retention in floodplain (eq. to reaction order)	-		explored
K_m	Li retention/dissolution saturating ratio in floodplain	-		explored
w	Flooding width (eq. to width of inundated area)	m	Spatially distributed	Martinez and Le Toan (2007)

Table 2: List of model main variables.

394

Variable	Description	Units
T	Surface air temperature	K
q	"Total" runoff (ie: precipitation minus evapo-transpiration)	m/y
E	Erosion rate	m/y
h	Regolith thickness	m
$F_{diss}(\mathrm{Li})$	Specific flux of lithium dissolved from primary phases (same value in *hillslope* and *floodplain* components)	mol/m^2/y
$F_{sp}^{reg}(\mathrm{Li})$	Specific flux of lithium retained in secondary phases in hillslopes	mol/m^2/y
$F_{sp}^{flood}(\mathrm{Li})$	Specific flux of lithium retained in secondary phases in floodplains	mol/m^2/y
$\delta_{riv}^{7}\mathrm{Li}$	Li isotopic ratio of water (either leaving the regolith of riverine water)	‰
$F_{riv}(\mathrm{Li})$	Flux of lithium carried by riverine water	mol/y

395

396

The required climatic fields, including temperature (T) and runoff (q), the erosion field (E), the water routing and the distribution of flooded areas are taken from global databases, reconstructions or remote sensing cartography.

Water routing has been taken from the Global Runoff Data Center at its original resolution 0.5°x0.5°.

The erosion field is taken from Ludwig and Probst (1998), still at its original resolution 0.5°x0.5°, and the climatic fields have been taken from the Climate Research Unit database and interpolated on the 0.5°x0.5° grid. The erosion field is shown on Fig. 2a.

This "floodplain" model component formulation depends *a priori* on both the "channel width" w, and the length of integration L. L depends on the size of each cell of the model grid and on the river sinuosity inside the cell. w represents the characteristic distance between the river bed and the characteristic flood distance. A careful study of Eq. 7 and 10 shows that the integrated values actually only depends on the products Lw. In other words, an integration path n times shorter gives exactly the same results if the width is n times wider. Then, it is meaningless to seek for the exact value of L and w in each cell. The product Lw is actually the area (in m^2) of the flooded continental surface that interacts with riverine water. It can be described as the average inundated area A_{flood}. In practice, we arbitrarily set L to the square root of the cell area: $L = \sqrt{A_{cell}}$, and then $w = A_{flood}/L$. The distribution of the inundated areas is estimated from satellite remote sensing. We apply the method developed by Martinez and Le Toan (2007) to two multi-temporal GRFM (Global Rain Forest Mapping) mosaics (100m resolution) derived from the J-ERS satellite Synthetic-Aperture Radar (SAR). One mosaic corresponds to the 1995-1996 dry season and the other corresponds to the wet season of the same hydrological year. This hydrological year is representative of the median climate condition of the Amazon basin (Abril et al., 2014). The map gathers the class "occasionally flooded" and "permanently flooded" defined by Martinez and Le Toan (2007), and account for both the open water bodies areas and flooded areas under vegetation. We thus consider the maximum extension of the floodplains for a standard hydrological year. Given the small number of hydraulic buildings and due to the low topographic gradients, this map can be considered as reproducible from one year to the other. The distribution of inundated areas are estimated from satellite remote sensing. We converted the high-resolution (~100m) contours of the inundated zones into a proportion of inundated area (in m^2/m^2) on each cell of the model mesh: A_{flood}/A_{cell} (Fig. 5 and Appendix A).

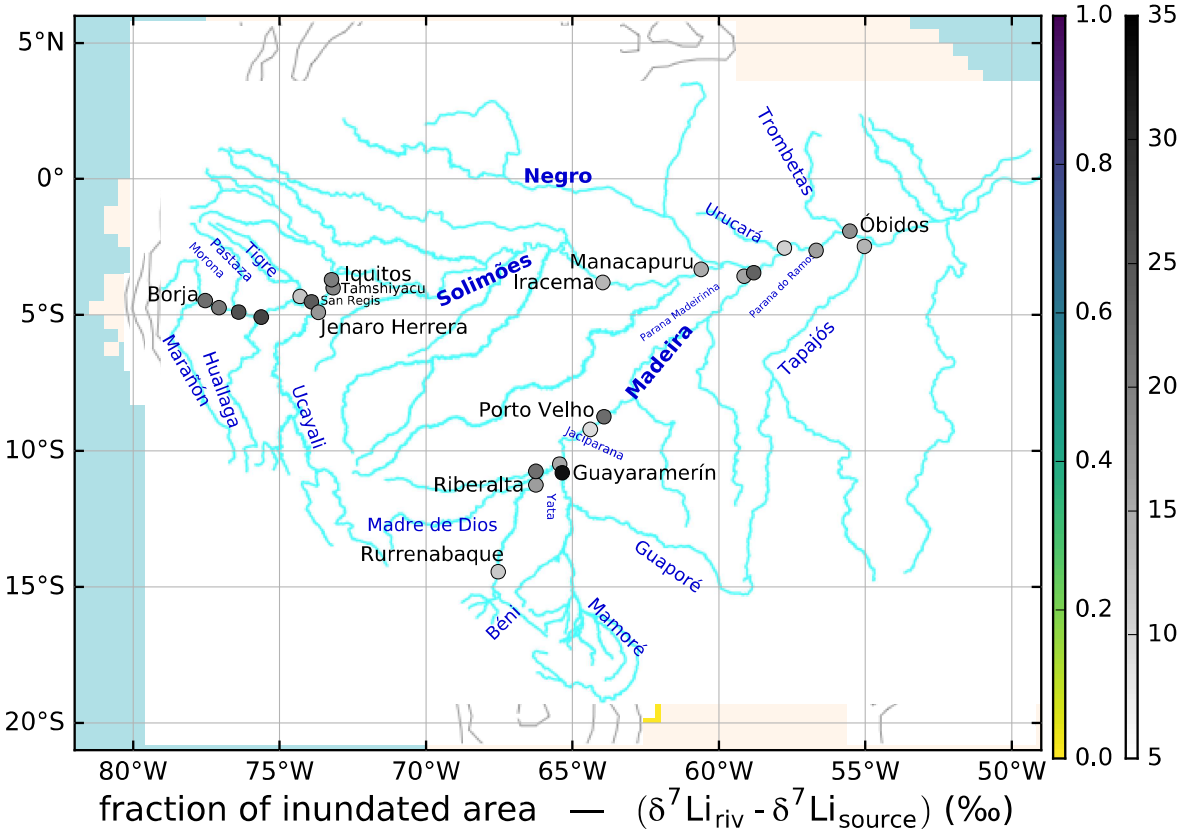

Figure 5: Map of the fraction of inundated area in each cell of the model grid (yellow to blue scale) and δ^7Li riverine minus the δ^7Li of the source rock (‰) from Dellinger et al. (2015; circles colored by the δ^7Li value, grayscale). The blue lines show the path of the main rivers; the white arrows show the water routing through the model grid; black contours are elevation isolines (500m, 1000m, 2000m, 4000m and 6000m). Names of the monitoring stations are written in black, river names in blue. When the station name is not specified, monitoring was done at the river outlet.

The last 4 parameters (τ_o, k_{sp}, a and K_m) do not have a value *a priori*, so we conducted an exploration.

One should notice that combining equations 2 (*hillslope* model) and 3 (regolith thickness) leads to:

$$\frac{F_{sp}^{reg}(\mathrm{Li})}{F_{diss}(\mathrm{Li})} = \left(1 + \frac{\tau_o}{\varphi h_o} \cdot q / \ln\left(k_{rp} \cdot q \cdot \exp\left(-\frac{E_A^{rp}}{R}\left(\frac{1}{T} - \frac{1}{T_0}\right)\right) / E\right)\right)^{-1}$$

This means that, once k_{rp} and E_A^{rp} fixed, the only thing that matters for the lithium retention ratio is the ratio $\tau_o/\varphi h_o$. In other words, there is no way to know the individual influences of h_o, φ and τ_o on the model. Then, we set the value of φ —regolith porosity— to 0.2 and only focus on τ_o (wich is the water residence time for which the dissolved δ^7Li reaches half of its maximum value, cf. Eq. 2).

Concerning the last "free" parameters, we conducted an exploration of the two-dimensional parameter space for each case (k_{sp} and a, 1st case, Eq. 8; or k_{sp} and K_m, 2nd, Eq. 9).

4. Results

4.1. Hillslopes

We first test the efficiency of the *regolith* model component, in simulating the effect of batch fractionation on the lithium isotopic composition of the rivers. Accordingly, the *regolith* component has been run alone without using the *floodplain* component. We compare our model results to a selection of data points documented by Dellinger et al. (2015) as the result of batch fractionation only. As erosion decreases from the Andes to the Amazonian plain, the regolithic cover becomes thicker (Eq. 3), the residence time of water becomes longer and consequently river δ^7Li should increase as more lithium is retained in secondary phase precipitation (Eq. 2 and 5). Such trends have been observed in the field by Dellinger et al. (2015) for 8 points of their database. Being the sole free parameter of our batch fractionation model, the half-retention residence time τ_o has been tuned so that two conditions are verified: (1) the model δ^7_{riv}Li - δ^7_{rock}Li versus the physical erosion matches the corresponding scatterplot of the data from Dellinger et al. (2015, Fig. 3a in their contribution), (2) the scatterplot of the simulated ratio $F_{sp}(\mathrm{Li})/F_{diss}(\mathrm{Li})$ versus physical erosion also matches the data scatterplot of Dellinger et al. (2015, Fig. 3b in their contribution). This is illustrated on Fig. 6 a and b. Here, only 3 of the 8 measurement sites can be precisely located within the model hydrographic network (the 5 others come from rivers too small to be accurately reproduced at the model resolution). We found that a τ_o value of 0.8 years leads to an acceptable match between model output and field data. The direct implication of this result is that our model formalism simulates correctly the batch fractionation process in the field. It might not be the unique solution, but all other parameters have been fixed to previously published values.

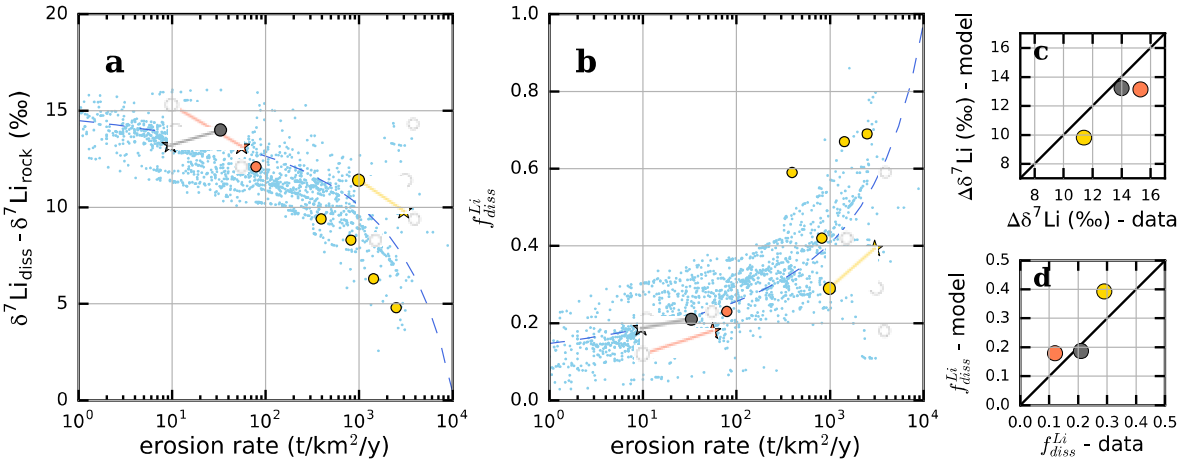

Figure 6: Comparison between the Dellinger et al. (2015) lithium data with the model output (without considering the potential role of inundated areas). Only the *hillslope* model is activated. Only "batch" fractionation is simulated : (a) scatterplot of the (δ^7_{riv}Li - δ^7_{rock}) versus erosion rate for data (circles colored accordingly to Dellinger et al. (2015), see Fig. 1) and model output. (b) fraction of dissolved lithium leaving the weathering system, f^{Li}_{diss} (Eq. 11) versus the erosion rate. The blue dots are the values calculated for each grid cell element. The stars display the model-calculated values for the three measurements stations that have been localized in the model hydrographic network. They are connected to the corresponding measured value by a solid line of the same color. The light colored circles correspond to rivers which are too small to be modeled using our typical resolution (see section 2 for more details) (c) and (d) scatterplots of data (x axis) versus model (y axis) for (c) the riverine δ⁷Li and (d) the fraction of dissolved lithium leaving the weathering system, f^{Li}_{diss}. Only the 3 stations localized in the model hydrographic network can be used here.

4.2. Coupling "*regolith*" and "*floodplain*" model components

Both lithium model components are now coupled. We use the value of the parameter τ_o calculated in the previous section. Contrary to the regolith model displaying only one free parameter (τ_o), the floodplain model has 2 free parameters (k_{sp} and a for case #1; k_{sp} and K_m for case #2), requiring a parameter optimization procedure.

We first test the case where Eq. 8 is used to compute $F_{sp}(\mathrm{Li})$ and the parameter optimization is performed by considering the entire river database. It is referred as case #1. The full model

is able to reproduce the two distinct trends observed by Dellinger et al. (2015) when plotting $\delta^7_{riv}\mathrm{Li}$ versus f^{Li}_{diss} (the ratio of the river flux of lithium at a given measurement site versus the upstream integrated fluxes of Li released by rock weathering):

$$f^{\mathrm{Li}}_{diss}(x) = \int_{\mathrm{upstr.}\ x}\left(F_{diss} - F_{sp}\right) / \int_{\mathrm{upstr.}\ x} F_{diss} = F_{riv}(x) / \int_{\mathrm{upstr.}\ x} F_{diss} \quad (11)$$

This is illustrated in Fig. 7 for parameterization case #1. The same result is also observed for the other parameterization (Eq. 9) (not shown). The grid cell where the "*regolith*" component of the numerical model is dominant plots along the batch fractionation line (black line in Fig. 7), with a fractionation factor Δ_{land} close to Dellinger et al. (2015)'s fit (17‰). The fact that data plot on a Δ=9‰ Rayleigh distillation trend is more surprising. The *floodplain* model component never simulates pure Rayleigh distillation except in areas where weathering rate is close to zero (corresponding to a $F_{diss}(\mathrm{Li})$ equal to zero).

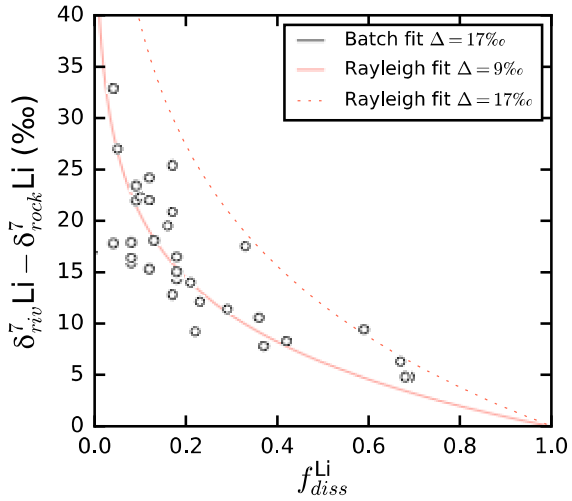

Figure 7: scatterplot of the riverine δ^7Li riverine minus the δ^7Li of the source rocks (y axis) as a function of the lithium riverine remaining fraction (f^{Li}_{diss}, Eq. 11, x axis). The Batch fractionation and Rayleigh distillation trends are represented by the black and red lines respectively. Colored circles are the Dellinger et al. (2015) data. Blue dots are model points. Only the case #1 is considered here: Eq. 8 for $F_{sp}(\mathrm{Li})$ with parameters optimised over the whole dataset (see section 4.6).

The highest $\delta^7_{riv}\mathrm{Li}$ are calculated for rivers flowing through inundated areas (see for instance Fig. 9, best-fit parameters of case #1). This result does not depend on the chosen parameterization for $F_{sp}(\mathrm{Li})$. The calculated isotopic composition of the dissolved Li in the Madeira river increases progressively during its journey through a large floodplain (Fig. 5). The highest $\delta^7_{riv}\mathrm{Li}$ are found downstream of the inundated area between 12°S and 15°S, and

the lower $\delta^7_{riv}\mathrm{Li}$ are found when the Béni river leaves the Andes. In the northern region of the Amazon watershed, the Solimões river seems to display an opposite trend: the highest measured $\delta^7_{riv}\mathrm{Li}$ are found at the entrance of the inundated area (25‰ and more), very close to the Andes (Huallaga, Pastaza, Morona, Marñón at Borja), and $\delta^7_{riv}\mathrm{Li}$ is lower downstream (Tamshiyacu, Iquitos) or for longer river path (Ucayali). Conversely, the model predicts values of 15‰, with a maximum of 20‰ at the feet of the Andes, before entering the floodplain.

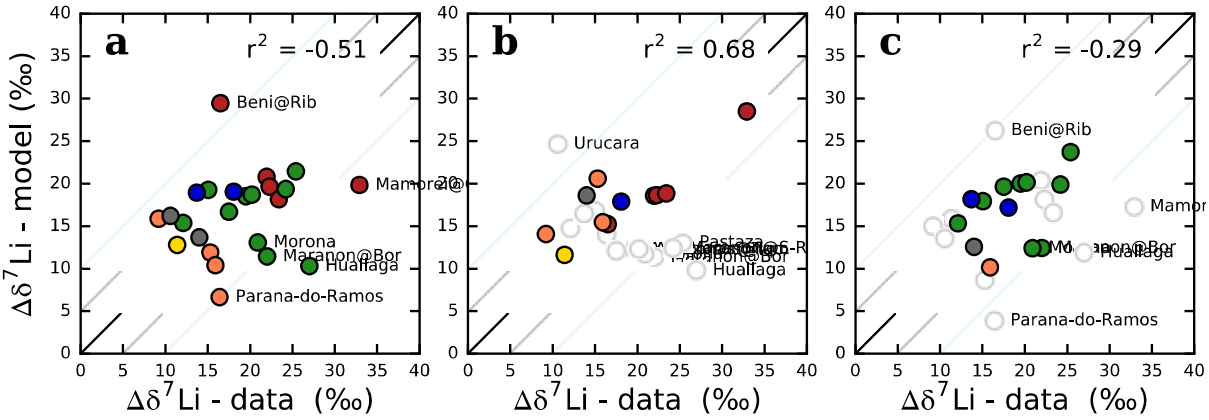

Figure 8: Data-model scatterplots when the model is run with the best-fit parameters for 3 cases: (a) Eq. 8 for $F_{sp}(\mathrm{Li})$ and optimization using all stations (case #1); (b): Eq. 9 for $F_{sp}(\mathrm{Li})$ and optimization on the Madeira only (case #2-M); (c) Eq. 8 for $F_{sp}(\mathrm{Li})$ and optimization on the Solimões only (case #1-S). On (b) and (c), the stations not used for the parameter optimization are drawn in transparency. The names of the stations where the misfits are greater than 7‰ (for δ^7_{riv} riv) are specified. Colour code follows Dellinger et al. (2015; see Fig. 1). Madeira tributaries are in yellow, red and orange (except Parana do Ramos), Solimões tributaries are displayed in green. On each panel, the bold line is the 1:1 line, the ligther lines denote the ±5% and ±10‰ mismatch. The coefficient of determination (r^2, see also Appendix D) is specified on each panel.

The optimization of the model parameters has been conducted using all the river samples available in Dellinger et al. (2015). Doing so, the model fails to explain the whole dataset at the scale of the Amazon basin. None of the tested combinations of parameters leads to a positive coefficient of determination (r^2), meaning that the mismatch between data and model is always greater than the variability of the data (Appendix D). The “best-fit” case shown in Fig. 8a ($r^2 = -0.51$) is actually a compromise between the two incompatible river’s

behaviours. In this configuration, the δ^7_{riv}Li of three Solimões tributaries are largely underestimated (by 15‰, 10‰ and 8‰ respectively): the Huallaga, the Marañón at Borja, and the Morona. This is because the "distillation rate" —given by the k_{sp}— is too low with respect to their small path through the inundated area. In parallel, the Béni at Riberalta δ^7Li value is overestimated by ~15‰ for the exactly opposite reason (rate of distillation too high with respect to its long path). The Mamoré at Guayaramerín is underestimated by ~10‰ despite its very long path though inundated areas. This paradoxical behaviour is in fact due to a distillation so efficient that the lithium concentration of the Mamoré becomes lower than the Guaporé's one at their confluence, although the Guaporé is providing a Li weathering flux several orders of magnitude lower than the Mamoré, and is actually negligible in term of chemical flux (see Fig. 2). The calculated isotopic signature of the Guaporé —much lower than the Mamoré's one— becomes dominant at the confluence of both rivers. The last outlier is the Parana do Ramos that is abnormally low with respect to all the rivers flowing in the plain. This is a consequence of a weathering increase shortly before the confluence with the Amazon mainstream (see Fig. 2b). The *floodplain* model responds to this increase of weathering with a drop in δ^7Li. This can be seen on the map of modelled δ^7Li with the "best-fit" parameters (Fig. 9).

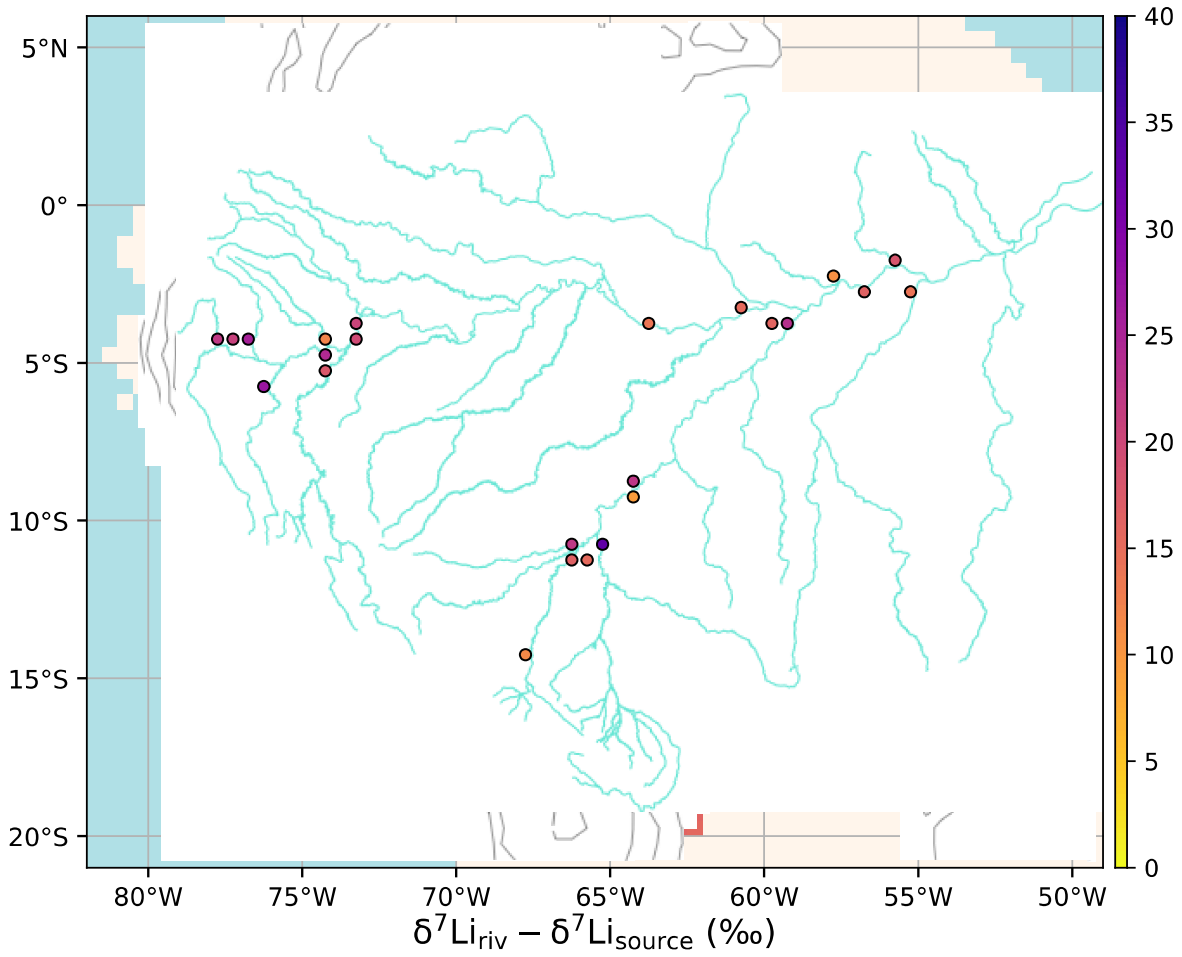

Figure 9: Map of δ^7Li riverine minus the δ^7Li of the source rock (‰) when the model is run with the best-fit parameters of case #1 (Eq. 8 for $F_{sp}(\mathrm{Li})$ and optimization on all stations). Circles shows the Dellinger et al. (2015) monitoring stations and are colored by the measured δ^7Li riverine minus the δ^7Li of the source rock. The blue lines show the path of the main rivers, the white arrows show water routing in the model grid, black contours are elevation isolines (500m, 1000m, 2000m, 4000m and 6000m).

If we use Eq. 9 for computing $F_{sp}(\mathrm{Li})$ (case #2), the results are not significantly improved (see Appendix D, best r^2 is -0.47). The best fit is found for higher K_m value (around 20). For such high values, Eq. 9 becomes equivalent to Eq. 8 in the linear case ($a = 1$).

4.3. Local optimizations:

603 The model output shows that lithium data from the Madeira and the Solimões cannot be
604 explained by a single mechanism, or at least, both systems cannot be described by a single
605 parameter combination. The "global" optimization performed in the previous section
606 represents a compromise where none of the river trend is correctly simulated (Fig. 8a).
607 Because of this apparent incompatibility, we performed a separate parameter optimization for
608 each basin. We optimized the parameters by minimizing the mismatch between the model
609 and the data, considering the points of the Madeira only (case -M), or those of the Solimões
610 only (case -S). We added —in both cases— the point downstream the confluence (Óbidos,
611 Tapajós and Parana Madeirinha). We removed —in both optimizations— two data points: the
612 Urucará and the Parana do Ramos. The Urucará is a shield river with a δ^7Li overestimated
613 by the model. Dellinger et al. have shown that shield rivers are impacted by clay dissolution
614 under the corrosive action of organic acids, leading to low δ^7Li. This is the case for the Negro
615 and Trombetas rivers, and we assume that it is also the case for the Urucará rivers, given its
616 location between the Negro and Trombetas. This clay dissolution process is not simulated
617 here, and we removed the Urucará from the optimization procedure. We removed the Parana
618 do Ramos because of the plausible artefact already mentioned (increase of weathering rate
619 before its mouth). Finally, for the optimization on the Solimões, we removed the data point of
620 the Huallaga. Indeed, this river displays a very high δ^7Li (27‰) despite the quasi-absence of
621 inundated area along its path. It has been shown that this river is affected by the dissolution
622 of evaporites (Dellinger et al., 2015; Moquet et al., 2011), with potentially high δ^7Li (Huh et
623 al., 1998).
624
625 For the optimization on the Madeira, the results are improved when using Eq. 9 for $F_{sp}(\mathrm{Li})$
626 (case #2-M). The best fit is reached for low K_m, around 6–7 ($r^2 = 0.68$). This corresponds to
627 a regime where $F_{sp}(\mathrm{Li})$ is limited by $F_{diss}(\mathrm{Li})$ (see Appendix D). As shown in Fig. 8b, the Béni
628 is no longer overestimated nor the Mamoré underestimated. The Parana do Ramos is well
629 predicted too though the optimization did not try to reduce its misfit. However, as expected,
630 most of the points from the Solimões are now underestimated.
631
632 When the optimization is performed on the Solimões tributaries, none of the two equations
633 for $F_{sp}(\mathrm{Li})$ (Eq. 8 or 9) yields reasonable results: r^2 remains negative in both cases. Eq. 8
634 (case #1-S) gives the "best" result (-0.29, shown in Fig. 8c). As in case #1, r^2 reaches a
635 plateau for high values of a (greater than 2, see Appendix D), making this optimization less
636 reliable. The Morona and Marañón at Borja are still underestimated. The Huallaga too but
637 that was expected because the parameter optimization does not try to reduce its mismatch
638 and this river is likely impacted by evaporite dissolution. Yet, for the first two, the

contributions from the dissolution of evaporites cannot be invoked as no significant dissolved flux from evaporites has been reported (Moquet et al., 2011). The behaviour of those three tributaries cannot be explained by the model coevally with the other points of the Solimões. Moreover, the data-model scatterplot of the current optimization (case #1-S, Fig. 8c) is very close to the one obtained with the whole dataset (case #1, Fig. 8a), and displays the same outliers: Béni at Riberalta, Mamoré at Guayaramerín and Parana do Ramos —in addition to the three Solimões tributaries.

While using Eq. 9 for $F_{sp}(\mathrm{Li})$ (case #2-S), r^2 is constantly increasing with K_m for the tested range (1–100, see Appendix D), as if the limitation by F_{diss} was inappropriate for this dataset. Indeed, Eq. 9 is equivalent Eq. 8 with $a = 1$ when K_m approaches infinity.

In an attempt to refine our modelling, we have constrained independently the range of parameters needed to explain the high δ^7Li values exhibited by the three Solimões tributaries. Then we test them for the whole dataset. For this, we first minimized the mismatch of these three points only (Appendix D), using Eq. 8 for $F_{sp}(\mathrm{Li})$. The results show that these three datapoints can be fitted by our modelling with a very low a (~0.3) and a very high k_{sp}. The k_{sp}value obtained here cannot be compared directly with other optimizations because it is directly correlated to a. Indeed, as $[\mathrm{Li}]_{riv}$ is lower than 1, increasing the exponent a requires to increase k_{sp} in order to keep the same order of magnitude for the product $k_{sp}[\mathrm{Li}]_{riv}{}^{a}$. For this reason, the plausible parameters plot along a straight line in $\{a, \log k_{sp}\}$ space, with a roughly similar slope in all optimizations (see Appendix D). One way to compare the k_{sp} of the different optimizations is to compare the intercept: for the minimum tested a (0.2), the values of k_{sp} we get are $\sim 3 \cdot 10^{-2}$ for cases #1 and #1-M, $\sim 5 \cdot 10^{-2}$ for case #1-S and $\sim 1 \cdot 10^{1}$ in the current optimization (Appendix D). By doing the same comparison at $a = 1$, we get a factor of 50. In conclusion, we see that explaining the values of the Marañón at Borja, the Huallaga and the Morona requires a kinetic of Li incorporation on secondary phases about 100 times faster compared to the three other optimizations. In that case, almost all the other rivers display an unrealistic δ^7Li, generally overestimated (Appendix D).

5. Discussion

The spatial fluctuations of river δ^7Li values along the course of the Madeira and its tributaries (Béni, Madre de Dios, Mamoré…) can be simulated by a batch fractionation in the regolith coupled to a Rayleigh distillation occurring in the plain flooded areas (case #2-M, Fig. 8b). Importantly, the model results show that the fit is better in the case #2 (Eq. 9 for F_{sp}) than in the case #1 (Eq. 8 for F_{sp}). Things are more complicated regarding the Solimões and its tributaries. High dissolved δ^7Li are rapidly reached at the feet of the Andes, well before the river reaches extensive flooded areas, a feature that our model cannot reproduce. The three highest riverine δ^7Li values have been measured in the Huallaga at mouth, in the Marañón at Borja and in the Morona at mouth. Among the Solimões monitoring stations, these three stations are the closest to the Andean range, the Huallaga having the highest measured δ^7Li. If these high values are caused by "Rayleigh" distillation in the floodplain, reaching high δ^7Li so upstream requires a kinetics of the interactions between water and the mineral phases (k_{sp}) 100 times more efficient compared to the other locations in the Amazon watershed. Furthermore, optimization of the model parameters using the Solimoes data shows that the best fit is obtained when Eq. 8 is used to describe the interaction between water and secondary phases in floodplains.

A contrasting behaviour between the Northern and the Southern parts of the Amazon watershed is thus identified. The isotopic signature of the Solimoes pole is best explained when the removal of lithium in floodplains (1) is a function of the amount of lithium carried by the upstream rivers (Eq. 8), (2) is not limited by the local dissolution of primary minerals, and (3) is operating at a fast rate (k_{sp}). Conversely, the isotopic signature of the Madeira is best explained when the floodplain interactions (1) are not only limited by the dissolved lithium carried by rivers, (2) but also by the release of lithium by the dissolution of fresh minerals incorporated in floodplain sediments, and (3) operate at a slower rate.

The suspended solids carried by the Solimoes and the Madeira derives from rocks of different original chemical composition (Viers et al., 2008). The lithology drained by the headwaters differs between the Solimoes and Madeira watersheds. The Andean headwaters of the Madeira drain shales, that are recycled sediments, depleted in cations but enriched in lithium and most of all, weakly weatherable. In contrast, in the Solimões river basin weathering budget is significantly influenced by igneous rocks (Dellinger et al. 2015), including a large contribution from volcanic rocks weathering. Weathering rate is doubtlessly not the same for these two basins (Moquet et al., 2011). We can speculate that because of lithological contrasts, the weathering of sediments eroded in the range occurs in the first

tenths of kilometres of the alluvial plain in the Solimões basin, whereas it occurs over larger distance in the Madeira basin (Bouchez et al., 2011).

The sediment load of the Solimoes and tributaries contains coarse solids supplied by the erosion of volcanic rocks exposed in the Andes, and includes the input of young basaltic products owing to the volcanic activity in Ecuador. The presence of unweathered minerals in the Solimoes suspended solids is probably the consequence of weathering conditions limited by unfavourable climate in the magmatic area from which they derive (Bouchez et al., 2011). Conversely, the suspended solids of the Madeira river and tributaries derive from Paleozoic sediments that originate from a cratonic rocks, and that have been impacted by several weathering cycles (Veizer and Janssen, 1979). The Chemical Index of Alteration ranges from 0.3 to 0.55 for the Madeira sediments, and is always below 0.3 for the Solimoes (Roddaz et al., 2014).

In the case of the Solimoes river and tributaries, the absence of limitation on the supply of lithium by local dissolution of minerals suggest that the sediments exported from the Andes contains easily weatherable materials. The model output suggest that the lithium is released and then removed at a fast rate owing to the fast dissolution rate of volcanic materials mixed in the sediments (Dessert et al., 2003). Those sediments also contain large amounts of smectite clay mineral, part of it being mechanically transported from uplands (Guyot et al., 2007; Dellinger et al., 2014). But smectite abundance in sediments is also rapidly rising with the distance from the mountain range, suggesting precipitation of smectite minerals (Guyot et al., 2007). The lithium might thus be supplied by upstream rivers, without being limited by local dissolution of primary minerals, and the abundance of clay minerals may result in both batch and “Rayleigh” distillation close to the Andes, before the water flows through large floodplains. In the Madeira, the sediments eroded upstream and accumulating in the Madeira floodplains are much more depleted in cations owing to their lithological origin. As a result, the lithium isotopic composition starts to rise during secondary mineral-water interactions only within extensive floodplains. The dimension of the flooded systems, and the residence time of water inside these flood plains, may compensate for the limitation in lithium supply by primary mineral dissolution inside the flood plain, allowing secondary phases to precipitate and the riverine δ^7Li to rise above the maximum value allowed by “batch” fractionation.

6. Limitations

745 Our results are highly dependent on the reliability of the calculated weathering field, where it
746 is considered that leaching or dissolution (in undersaturated conditions) is congruent
747 (F_{diss}(Li) is set proportional to weathering rate). This seems reasonable based on recent
748 experimental investigations (e.g. Pistiner and Henderson, 2003; Verney-Carron et al., 2011;
749 Wimpenny et al., 2010a; Ryu et al., 2014). Moreover, we assumed a uniform weathering rate
750 inside each cell, even if the cell is partly flooded. However, the weathering rate could be
751 higher or lower in the flooded part of the grid cell, compared to the weathering contribution of
752 the non-flooded part of the grid cell. The release of lithium by weathering may depend on the
753 nature of deposited sediments, being more or less weatherable. Therefore, the dissolution
754 rates within the flooded area of the model remains poorly constrained. If the weathering rates
755 in flooded area differ significantly from the weathering rate outside the flooded area, nothing
756 can be said about the relative efficiency of Eq. 9 versus Eq. 8.
757
758 The processes at play within the floodplains are not fully identified. Here we propose a
759 simple formalism to describe those processes (Eq. 8 and 9), and we postulate, in agreement
760 with Dellinger et al. (2015) that the enrichment of riverine waters occur in the flood plains.
761 Yet the enrichment in ^{7}Li of the water depends probably also on the nature of the sediments
762 being stored (as we discussed above), on their reactivity, and on the size and geometry of
763 the aquifer. Here we only account for the lateral extension of the flooded area to modulate
764 the residence time of water.
765
766 The climate is not uniform over the Amazon watershed. The Solimões flows under a tropical
767 rainforest climate, with very low seasonality, whereas the Madeira, located southward, has a
768 tropical monsoon climate with more pronounced seasonal contrast. Although no clear
769 seasonal fluctuations in the riverine isotopic composition have been reported up to now,
770 seasonal precipitations may explain a lower lithium uptake rate, because flooding areas are
771 inundated only for a few months a year. Yet, alternate wet and dry period could also lead to
772 more intense distillation via strong evaporation in varseas disconnected from river paths
773 during the dry season. The influence of seasonality is far from being understood.
774
775 Another possibility is that Rayleigh distillation does not take place only in inundated areas,
776 but within the whole basin. Several studies have highlighted high δ^{7}Li values in mountainous
777 rivers (Burton and Vigier, 2012; Schmitt et al., 2012). Some of these high values cannot be
778 explained by batch fractionation as underlined in the introduction. Recent δ^{7}Li values
779 published for mountainous rivers are rather low. While these new data suggest that high δ^{7}Li
780 in mountains might be an exception rather than a common feature, high values must still be
781 explained. Colluviums are a possible site for lithium distillation in mountains: if river waters

flow through colluviums, a reactive transport concept would makes sense: lithium would dissolve upstream, and be incorporated into colluviums, leading to a pseudo-distillation just like in *floodplain* model, although shorter residence time of the waters are expected compared to the floodplain environments. The existence of such a “distillation” process along the groundwater path has been postulated and simulated by Bohlin and Bickle (2019) for kinetically-limited weathering environment. Still we need to further understand why colluvium would play a more important role in the Solimões Li cycle and not in the Madeira one.

7. Conclusions

In the present study, we explore the processes controlling the elementary and isotopic cycle of the lithium in a continental-scale watershed: the Amazonian basin. We build a numerical model specifically designed to simulate the processes at play in vertical weathering profiles, and coupled it to an horizontal reactive-transport model. The model is able to simulate the impact of the formation of weathering profiles on the lithium isotopic composition of the rivers, as well as the role of floodplains. The model takes advantage on the existence of spatially distributed sites where the riverine lithium has been monitored, from the Andes to the outlet in the Atlantic ocean.

We identify two different regimes in the Amazon basin. In the southern part of the basin (Madeira basin), the evolution of the riverine lithium isotopic composition can be explained by the production of lithium by weathering reactions inside the regolith, with a fractionation occurring during the precipitation of secondary mineral phases. Then, interactions between the water and the secondary mineral phases within floodplains generate a Rayleigh distillation process explaining high isotopic values for dissolved riverine lithium. This scenario was previously proposed by Dellinger et al. (2015) based on river sampling. In the Northern part of the watershed (Solimões and tributaries), this scenario cannot account for the lithium isotopic composition of the tributaries of the Amazon. Indeed, the Huallaga, Marañón at Borja and Morona display high isotopic values well before they flow through the inundated area in the flood plain. An in-depth study of the model parameters suggests that the nature of the bedrock eroded in the North of the Andes (fresh volcanic materials) and transported downstream may impact strongly the δ^7Li of the tributaries of the Solimoes. We suggest that the efficient weathering of this material directly at the feet of the Andes, together with reported precipitation of smectites, allows the riverine δ^7Li to rise upstream of the floodplains. But, in its present state, the model failed at reproducing the measured upstream high isotopic values without accelerating the kinetics of the reactions up to non-reasonable values. In

addition, we suggest that two other factors should be explored in more detailed in future modelling: the amplitude of the climatic seasonal fluctuations (less pronounced in the Northern part of the watershed), and the possibility for Rayleigh distillation processes in uplands when water flows through colluvions or along the flow path of the groundwaters.

Our study shows that the lithium continental cycle is not fully understood yet, at least for the biggest watershed on Earth. More data are obviously needed to constrain models. More sampling of the riverine δ^7Li, especially in the mountainous tributaries, would help at identifying where the isotopic ratios increases. We also think that data relative to the lithology must be gathered, including rock type, dissolution rates, lithium content and isotopic signature. This has implications on the interpretation of the oceanic lithium isotopic composition in terms of past weathering. The variability of the lithium isotopic signature at the outlet of the same mountain range (the Andes) suggests that the role of mountains on this tracer is not well-constrained yet, and consequently their impact on the global carbon cycle and other major chemical species are still to be refined.

8. Acknowledgments

The authors thank Jérôme Gaillardet, Jacques Schott, Martin Roddaz, Jean-Loup Guyot, Mathieu Dellinger for helpful discussions. Two anonymous reviewers greatly help at improving this manuscript.

9. Declaration of interest

The authors declare they have no conflict of interest.

10. Funding

This research was supported by the ANR INTOCC.

References:

Abril, G., Martinez, J.-M., Artigas, L.F., Moreira-Turcq, P., Benedetti, M.F., Vidal, L.,

Meziane, T., Kim, J.-H., Bernardes, M.-C., Savoye, N., Deborde, J., Lima Souza, E., Albéric, P., Landim de Souza, M.F., Roland, F., 2014. Amazon River carbon dioxide outgassing fuelled by wetlands. Nature, 505, 395-398. https://doi.org/10.1038/nature12797

Bagard, M.-L., West, A.J., Newman, K., Basu, A.R., 2015. Lithium isotope fractionation in the Ganges–Brahmaputra floodplain and implications for groundwater impact on seawater isotopic composition. Earth Planet. Sci. Lett. 432, 404–414. https://doi.org/10.1016/j.epsl.2015.08.036

Bohlin, M.S., Bickle, M.J., 2019. The reactive transport of Li as a monitor of weathering processes in kinetically limited weathering regimes. Earth Planet. Sci. Lett., 511, 233-243lanet. Sci. Lett. 432, 404–414. https://doi.org/10.1016/j.epsl.2019.01.034

Bouchez, J., Gaillardet, J., France-Lanord, C., Maurice, L., Dutra-Maia, P., 2011. Grain size control of river suspended sediment geochemistry: clues from the Amazon River depth profiles. Geochem. Geophys. Geosys., 12, doi: 10.1029/2010GC003380.

Bouchez, J., von Blanckenburg, F., Schuessler, J.A., 2013. Modeling novel stable isotope ratios in the weathering zone. Am. J. Sci. 313, 267–308. https://doi.org/10.2475/04.2013.01

Burton, K.W., Vigier, N., 2012. Lithium Isotopes as Tracers in Marine and Terrestrial Environments, in: Baskaran, M. (Ed.), Handbook of Environmental Isotope Geochemistry. Springer Berlin Heidelberg, Berlin, Heidelberg, pp. 41–59. https://doi.org/10.1007/978-3-642-10637-8_4

Carretier, S., Goddéris, Y., Delannoy, T., Rouby, D., 2014. Mean bedrock-to-saprolite conversion and erosion rates during mountain growth and decline.Geomorphology, 209, 39-52

Dellinger, M., Gaillardet, J., Bouchez, J., Calmels, D., Galy, V., Hilton, R.G., Louvat, P., France-Lanord, C., 2014. Lithium isotopes in large rivers reveal the cannibalistic nature of modern continental weathering and erosion. Earth Planet. Sci. Lett. 401, 359–372. https://doi.org/10.1016/j.epsl.2014.05.061

Dellinger, M., Gaillardet, J., Bouchez, J., Calmels, D., Louvat, P., Dosseto, A., Gorge, C., Alanoca, L., Maurice, L., 2015. Riverine Li isotope fractionation in the Amazon River basin controlled by the weathering regimes. Geochim. Cosmochim. Acta 164, 71–93. https://doi.org/10.1016/j.gca.2015.04.042

Dessert, C., Dupré, B., Gaillardet, J., François, L.M., Allègre, C.J., 2003. Basalt weathering laws and the impact of basalt weathering on the global carbon cycle. Chem. Geol., 202, 257-273.

Dupuis, R., Benoit, M., Tuckerman, M.E., Méheut, M., 2017. Importance of a Fully Anharmonic Treatment of Equilibrium Isotope Fractionation Properties of Dissolved Ionic Species As Evidenced by Li^+ (aq). Acc. Chem. Res. 50, 1597–1605. https://doi.org/10.1021/acs.accounts.6b00607

Gabet, E.J., Mudd, S.M., 2009. A theoretical model coupling chemical weathering rates with denudation rates. Geology 37, 151–154. https://doi.org/10.1130/G25270A.1

Guyot, J.L., Jouanneau, J.M., Soares, L., Boaventura, G.R., Maillet, N., Lagane, C., 2007. Clay mineral composition of river sediments in the Amazon Basin. Catena, 71, 340-356.

Henchiri, S., Gaillardet, J., Dellinger, M., Bouchez, J., Spencer, R.G.M., 2016. Riverine dissolved lithium isotopic signatures in low-relief central Africa and their link to weathering regimes: Geophys. Res. Lett. 43, 4391–4399.

https://doi.org/10.1002/2016GL067711
Hindshaw, R.S., Tosca, R., Goût, T.L., Farnan, I., Tosca, N.J., Tipper, E.T., 2019. Experimental constraints on Li isotope fractionation during clay formation. Geochim. Cosmochim. Acta, 250, 219-237. https://doi.org/10.1016/j.gca.2019.02.015
Huh, Y., Chan, L.-H., Edmond, J.M., 2001. Lithium isotopes as a probe of weathering processes: Orinoco River. Earth Planet. Sci. Lett. 194, 189–199. https://doi.org/10.1016/S0012-821X(01)00523-4
Huh, Y., Chan, L.-H., Zhang, L., Edmond, J.M., 1998. Lithium and its isotopes in major world rivers: implications for weathering and the oceanic budget. Geochim. Cosmochim. Acta 62, 2039–2051. https://doi.org/10.1016/S0016-7037(98)00126-4
Kısakűrek, B., James, R.H., Harris, N.B.W., 2005. Li and d^{7}Li in Himalayan rivers: Proxies for silicate weathering? Earth Planet. Sci. Lett. 237, 387–401. https://doi.org/10.1016/j.epsl.2005.07.019
Li, G., West, A.J., 2014. Evolution of Cenozoic seawater lithium isotopes: Coupling of global denudation regime and shifting seawater sinks. Earth Planet. Sci. Lett. 401, 284–293. https://doi.org/10.1016/j.epsl.2014.06.011
Ludwig, W., Probst, J.-L., 1998. River sediment discharge to the oceans; present-day controls and global budgets. Am. J. Sci. 298, 265–295. https://doi.org/10.2475/ajs.298.4.265
Maffre, P., Ladant, J.-B., Moquet, J.-S., Carretier, S., Labat, D., Goddéris, Y., 2018. Mountain ranges, climate and weathering. Do orogens strengthen or weaken the silicate weathering carbon sink? Earth Planet. Sci. Lett. 493, 174–185. https://doi.org/10.1016/j.epsl.2018.04.034
Martinez, J., Le Toan, T., 2007. Mapping of flood dynamics and spatial distribution of vegetation in the Amazon floodplain using multitemporal SAR data. Remote Sens. Environ. 108, 209–223. https://doi.org/10.1016/j.rse.2006.11.012
Millot, R., Scaillet, B., Sanjuan, B., 2010a. Lithium isotopes in island arc geothermal systems: Guadeloupe, Martinique (French West Indies) and experimental approach. Geochim. Cosmochim. Acta 74, 1852–1871. https://doi.org/10.1016/j.gca.2009.12.007
Millot, R., Vigier, N., Gaillardet, J., 2010b. Behaviour of lithium and its isotopes during weathering in the Mackenzie Basin, Canada. Geochim. Cosmochim. Acta 74, 3897–3912. https://doi.org/10.1016/j.gca.2010.04.025
Moquet, J.-S., Crave, A., Viers, J., Seyler, P., Armijos, E., Bourrel, L., Chavarri, E., Lagane, C., Laraque, A., Casimiro, W.S.L., Pombosa, R., Noriega, L., Vera, A., Guyot, J.-L., 2011. Chemical weathering and atmospheric/soil CO_2 uptake in the Andean and Foreland Amazon basins. Chem. Geol. 287, 1–26. https://doi.org/10.1016/j.chemgeo.2011.01.005
Moquet, J.-S., Guyot, J.-L., Crave, A., Viers, J., Filizola, N., Martinez, J.-M., Oliveira, T.C., Sánchez, L.S.H., Lagane, C., Casimiro, W.S.L., Noriega, L., Pombosa, R., 2016. Amazon River dissolved load: temporal dynamics and annual budget from the Andes to the ocean. Environ. Sci. Pollut. Res. 23, 11405–11429. https://doi.org/10.1007/s11356-015-5503-6
Oliva, P., Viers, J., Dupré, B., 2003. Chemical weathering in granitic environments. Chem. Geol., 202, 225-256.
Pistiner, J.S., Henderson, G.M., 2003. Lithium-isotope fractionation during continental weathering processes. Earth Planet. Sci. Lett. 214, 327–339. https://doi.org/10.1016/S0012-821X(03)00348-0

956 Pogge von Strandmann, P.A.E., Frings, P.J., Murphy, M.J., 2017. Lithium isotope
957 behaviour during weathering in the Ganges Alluvial Plain. Geochim.
958 Cosmochim. Acta 198, 17–31. https://doi.org/10.1016/j.gca.2016.11.017
959 Pogge von Strandmann, P.A.E., Henderson, G.M., 2015. The Li isotope response to
960 mountain uplift. Geology 43, 67–70. https://doi.org/10.1130/G36162.1
961 Roddaz, M., Viers, J., Moreira-Turcq, P., Blondel, C., Sondag, F., Guyot, J.-L.,
962 Moreira, L., 2014. Evidence for the control of the geochemistry of Amazonian
963 floodplain sediments by stratification of suspended sediments in the Amazon.
964 Chem. Geol., 387, 101-110.
965 Riebe, C.S., Kirchner, J.W., Finkel, R.C., 2004. Erosional and climatic effects on
966 long-term chemical weathering rates in granitic landscapes spanning diverse
967 climate regimes. Earth Planet. Sci. Lett. 224, 547–562.
968 https://doi.org/10.1016/j.epsl.2004.05.019
969 Ryu, J.-S., Vigier, N., Lee, S.-W., Lee, K.-S., Chadwick, O.A., 2014. Variation of
970 lithium isotope geochemistry during basalt weathering and secondary mineral
971 transformations in Hawaii. Geochim. Cosmochim. Acta 145, 103–115.
972 https://doi.org/10.1016/j.gca.2014.08.030
973 Schmitt, A.-D., Vigier, N., Lemarchand, D., Millot, R., Stille, P., Chabaux, F., 2012.
974 Processes controlling the stable isotope compositions of Li, B, Mg and Ca in
975 plants, soils and waters: A review. Comptes Rendus Geosci. 344, 704–722.
976 https://doi.org/10.1016/j.crte.2012.10.002
977 Stallard, R.F., Edmond, J.M., 1983. Geochemistry of the Amazon: 2. The influence of
978 geology and weathering environment on the dissolved load. J. Geophys.
979 Res. Oceans 88, 9671–9688. https://doi.org/10.1029/JC088iC14p09671
980 Teng, F.-Z., McDonough, W.F., Rudnick, R.L., Dalpé, C., Tomascak, P.B., Chappell,
981 B.W., Gao, S., 2004. Lithium isotopic composition and concentration of the
982 upper continental crust. Geochim. Cosmochim. Acta 68, 4167–4178.
983 https://doi.org/10.1016/j.gca.2004.03.031
984 Teng, F.-Z., Rudnick, R.L., McDonough, W.F., Wu, F.-Y., 2009. Lithium isotopic
985 systematics of A-type granites and their mafic enclaves: Further constraints
986 on the Li isotopic composition of the continental crust. Chem. Geol. 262,
987 370–379. https://doi.org/10.1016/j.chemgeo.2009.02.009
988 Veizer, J., Jansen, J.L., 1979. Basement and sedimentary recycling and continental
989 evolution. J. Geology, 87: 341-370.
990 Verney-Carron, A., Vigier, N., Millot, R., 2011. Experimental determination of the role
991 of diffusion on Li isotope fractionation during basaltic glass weathering.
992 Geochim. Cosmochim. Acta 75, 3452–3468.
993 https://doi.org/10.1016/j.gca.2011.03.019
994 Viers, J., Roddaz, M., Filizola, N., Guyot, J.-L., Sondag, F., Brunet, P., Zouiten, C.,
995 Boucayrand, C., Martin, F., Boaventura, G. R., 2008. Seasonal and
996 provenance controls on Nd-Sr isotopic compositions of Amazon rivers
997 suspended sediments and implications for Nd and Sr fluxes exported to the
998 Atlantic Ocean. Earth Planet. Sci. Lett., 274, 511-523.
999 Vigier, N., Decarreau, A., Millot, R., Carignan, J., Petit, S., France-Lanord, C., 2008.
1000 Quantifying Li isotope fractionation during smectite formation and
1001 implications for the Li cycle. Geochim. Cosmochim. Acta 72, 780–792.
1002 https://doi.org/10.1016/j.gca.2007.11.011
1003 Vigier, N., Gislason, S.R., Burton, K.W., Millot, R., Mokadem, F., 2009. The
1004 relationship between riverine lithium isotope composition and silicate
1005 weathering rates in Iceland. Earth Planet. Sci. Lett. 287, 434–441.

https://doi.org/10.1016/j.epsl.2009.08.026
West, A., Galy, A., Bickle, M., 2005. Tectonic and climatic controls on silicate weathering. Earth Planet. Sci. Lett. 235, 211–228. https://doi.org/10.1016/j.epsl.2005.03.020
West, A.J., 2012. Thickness of the chemical weathering zone and implications for erosional and climatic drivers of weathering and for carbon-cycle feedbacks. Geology 40, 811–814. https://doi.org/10.1130/G33041.1
Wimpenny, J., Gíslason, S.R., James, R.H., Gannoun, A., Pogge Von Strandmann, P.A.E., Burton, K.W., 2010a. The behaviour of Li and Mg isotopes during primary phase dissolution and secondary mineral formation in basalt. Geochim. Cosmochim. Acta 74, 5259–5279. https://doi.org/10.1016/j.gca.2010.06.028
Wimpenny, J., James, R.H., Burton, K.W., Gannoun, A., Mokadem, F., Gíslason, S.R., 2010b. Glacial effects on weathering processes: New insights from the elemental and lithium isotopic composition of West Greenland rivers. Earth Planet. Sci. Lett. 290, 427–437. https://doi.org/10.1016/j.epsl.2009.12.042

Appendix A: stations and measurements of HYBAM database — correction method

The HYBAM (HYdrologie du Bassin AMazonien) observatory monitors daily discharge, monthly chemical compositions of rivers and the carried suspended load (with a ten-days frequency) over a network of hydrological stations distributed in the Amazonian basin from the Andes to the outlet. These time series are freely available from the HYBAM observatory website (http://www.ore-hybam.org/).

We use the erosion flux (sediment transport) and dissolved cation flux released by silicate weathering reconstructed by Moquet et al. (2011) for the 26 Andean basins of the Amazon. The silicate weathering fluxes are corrected for atmospheric inputs. (Moquet et al., 2011). Ten additional stations have been added to the present study (Moquet et al., 2016), using the same correction procedure for the atmospheric input than Moquet et al. (2011). For each sampling station, we subtract the flux from the upstream stations in order to get fluxes from non-overlapping areas. The map of these non-overlapping watersheds and their corresponding stations is shown in Fig. A1. Eight watersheds have been removed from the present analyses because the subtraction procedure gave aberrant fluxes due to the proximity of the upstream and downstream stations considered to calculate the sub-basin flux (CES, EXU, FAZ, OBI, PVE, SRE, TAB, TAM). Their watersheds and names appears in transparency on Fig. A1.

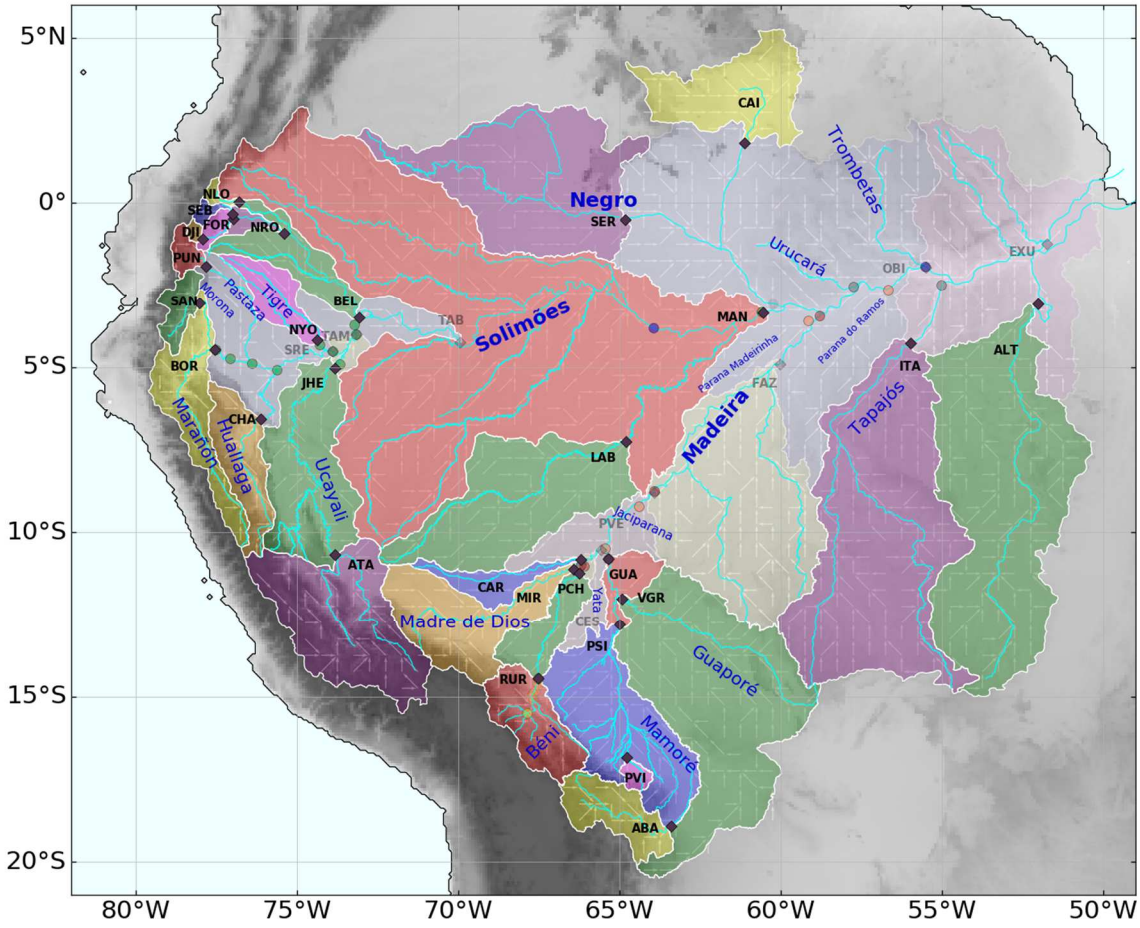

Figure A1: Map of the Dellinger et al. (2015) stations (colored circles), the HYBAM stations (black diamonds) and the corresponding watersheds (colored shades). Those put in transparencies have been used in the correction procedure, because the fluxes difference (upstream minus downstream) was lower than the fluxes uncertainties. The abbreviations of HYBAM stations follow Moquet et al. (2016).

These measured fluxes are used to correct both the erosion and weathering fields used by the model. First, the watershed are converted into the regular 0.5°x0.5° model grid as follow: for each station k, for each cell of the grid $\{i,j\}$ (ie: cell located at the i^{th} column and the j^{th} row), we computed the area common to the watershed *k* and the grid cell $\{i,j\}$: $A_{i,j}^{k}$. The total area of the cell is $A_{i,j}^{tot}$.

The modeled erosion flux at the station k is then:

$$F_k = \sum_{i,j} E_{i,j} A_{i,j}^{k}$$

where $E_{i,j}$ is the erosion rate field as used by the lithium model.

F_k^{dat} is the erosion flux measured at the station k. The simplest way to correct the erosion $E_{i,j}$ would be to multiply each cell of the considered watershed by the ratio of the measured erosion flux at station k versus the model integrated erosion flux at the same station. The correction would thus be uniform over one given watershed:

$$E_{i,j}^{corr} = E_{i,j} \cdot \left(F_k^{dat}/F_k\right)$$

The problem is that many cells intercept several watersheds. They would see their erosion rate corrected several times, and these corrections are uncompatible. We overcame this issue by correcting *iteratively* the whole erosion field.

Starting with:

$$E_{i,j}^{0} = E_{i,j}$$

We iterated as follow:

$$F_k^n = \sum_{i,j} E_{i,j}^n A_{i,j}^k$$

$$E_{i,j}^{n+1} = E_{i,j}^n \prod_k \left(F_k^{dat}/F_k^n\right)^{A_{i,j}^k/A_{i,j}^{tot}}$$

The exponent $A_{i,j}^k/A_{i,j}^{tot}$ ensures that cells not intercepting the watershed k will not be modified by F_k^{dat}, and also provides a smoother transition for cells at the boundary between several watersheds. Note that the order of the stations (k) used for the computation has no importance because the terms of the product are interchangeable.

This process converges toward a stable corrected field $E_{i,j}^{\infty}$ that verifies —for each k— the relation $F_k^{\infty} = \sum_{i,j} E_{i,j}^{\infty} A_{i,j}^k = F_k^{dat}$. In practice, 10 iterations are sufficient to get close to this equality.

The corrected erosion field is used to compute the silicate cations dissolution field (Eq. 1), which is then corrected by the HYBAM measurements of silicate cations using exactly the same method. Finally, the lithium dissolution is computed with this corrected cation dissolution rate assuming a constant lithium-cation ratio in source rock:

$$F_{diss}(\mathrm{Li}) \quad = \quad \frac{\chi_{\mathrm{Li}}}{\chi_{cat}} F_{diss}^{corr}(\mathrm{cat})$$

Note that the field of cation dissolution rate computed in Maffre et al., (2018) —with optimization only on HYBAM data— was already in agreement with data ($r^2 = 0.45$), most of rivers misfit the data by less than an factor 2.

Appendix B: theoretical behaviour of the "floodplain" model

Fig. B1 shows an idealized case where the floodplain model is run alone, on a 1D river profile with constant water discharge and constant width w. The parameters and the lithium dissolution flux (F_{diss}, forcing of the model) have been set arbitrarily to illustrate the model behaviour. F_{diss} is set constant over the first 1000 km of the river flow. The model is initialized (at $x = 0$) with no lithium in the water (except when k_{sp} is modified, it is initialized with equilibrium conditions). Whatever the equation chosen for $F_{sp}(\mathrm{Li})$, or the parameter values, the model reaches the equilibrium: lithium concentration increase until F_{sp} balances F_{diss} (Fig. B1 a and c), and concurrently, $\delta^7_{riv}\mathrm{Li}$ increases from bedrock value ($\delta^7_{rock}\mathrm{Li}$) towards its equilibrium value: $\delta^7_{rock}\mathrm{Li} + \Delta_{land}$ (Fig. B1 b and d).

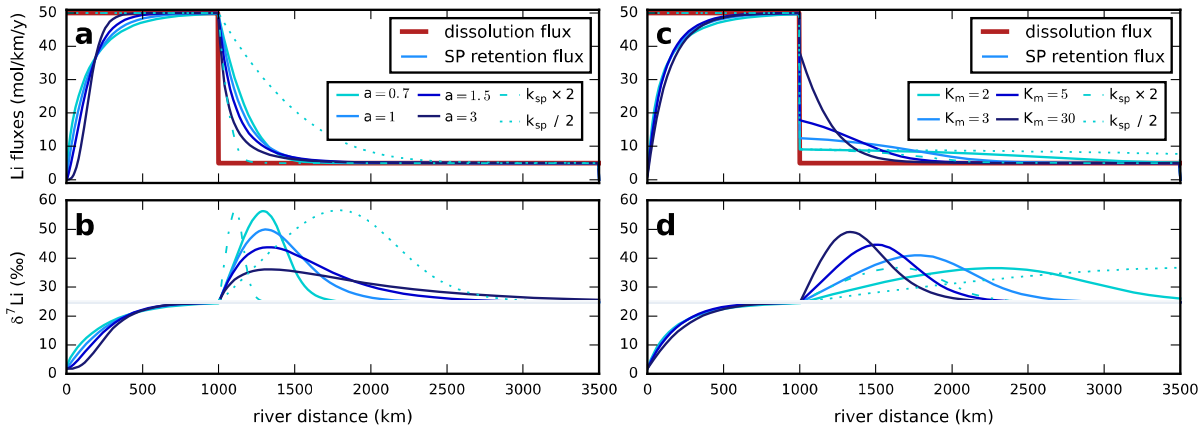

Figure B1: Examples of the 1D *floodplain* model response to a prescribed decreasing step of the supply of dissolved Li by chemical weathering of the bedrock (red thick line in panels a and b). This flux is reduced by 90% at 1000km, after the river reached its equilibrium state (in all cases). The model is initialized with no lithium in river water, and the δ^7Li of source rock is set at 0‰. Moreover, a constant flood width w (30km) and water discharge (20 km^3/y) along the river has been chosen for these examples. (a) and (b): lithium fluxes (mol/km/y): dissolution ($F_{diss}(\mathrm{Li})$, prescribed, red line) and retention in secondary phases ($F_{sp}(\mathrm{Li})$, all blue lines). (c) and (d): riverine δ^7Li. (a) and (c) correspond to case #1 (Eq. 8 for $F_{sp}(\mathrm{Li})$), (b) and (d) to case #2 (Eq. 9 for $F_{sp}(\mathrm{Li})$). In all panels, the different solid blue lines correspond to different values for the second parameter (a for case #1, panels a and c; K_m for case #2, panels b and d). The kinetics constant k_{sp} is modified with the second parameter in order to keep the same response time. For the dashed and dotted curves, the kinetics constant k_{sp} has been multiplied or divided by 2 with respect to the "reference" case (solid curve of the same color) without changing the second parameter. For this cases only, the model is

initiated with equilibrium values because response time has changed. When k_{sp} is divided by 2, the equilibrium would not have been reached before the perturbation at 1000km.

At $x = 1000\text{km}$ (once the river is at steady state), we force F_{diss} to decrease by –90%, an arbitrary value chosen to generate a significant response of the model. This drop in F_{diss} is expected when the river leaves the mountain range (or the foreland) and reaches the floodplain —though rivers are not necessarily at steady-state at that moment. The imbalance between F_{sp} and F_{diss} leads to a net uptake of Li, until F_{sp} decreases and balance F_{diss} again. This uptake (F_{sp} greater than F_{diss}) triggers first a rise of $\delta^7_{riv}\text{Li}$ before it decreases towards its steady state value. This behaviour is independent of the equation used to simulate F_{sp} and of the chosen parameterization. The intensity of the peak directly depends on the intensity of the drop in F_{diss}, it also depends on the "second" parameter: a ("reaction order", first case, Eq. 8, Fig. B1a–b) or K_m (saturating SP/diss ratio, second case, Eq. 9, Fig. B1c–d), but it is almost insensitive to the kinetics constant k_{sp}.

In the first case (case #1), low values for a generate a pronounced $\delta^7_{riv}\text{Li}$ peak, but rapidly relaxing to equilibrium. Conversely, high values for a generate low peak, with the maximum slightly delayed and relaxation to equilibrium much slower. a also controls the symmetry of the peak: it is symmetrical for $a = 1$, decreasing faster than increasing for $a < 1$ and decreasing slower than increasing for $a > 1$ (Fig. B1b). In the second case (case #2), the low K_m generates low, delayed and asymmetrical peak (decreasing faster than increasing). At high K_m, the model becomes equivalent to the first case with $a = 1$ (Fig. B1a).

In both cases, modifying the kinetics constant k_{sp} make the peak sharper or wider without changing its shape, or intensity. This behaviour is theoretically expected if we have $F_{sp} \gg F_{diss}$ and in the second case $K_m F_{diss} \gg k_{sp}[\text{Li}]_{riv}$ —meaning F_{sp} is not saturated by F_{diss}. With these conditions, rescaling k_{sp} by a factor n is equivalent to rescaling x by a factor $1/n$.

Appendix C: numerical resolution of lithium models.

Cells of the model mesh are first ordered from upstream to downstream along the specified drainage network and then treated in that order, so that their incoming water fluxes and material are known. In the drainage network we used, each cell is connected to a unique downstream cell, and the following equations involve this assumption. Once the sorting complete, the four integration steps are computed cell by cell in the following order. (*H* denotes *hillslope* model and *F floodplain* model):

1. Running the *hillslope* model (Eq. 2 and 5) and computing $F_{riv}(\mathrm{Li})_H$ and $\delta^7_{riv}\mathrm{Li}_H$

2. Averaging the output of all upstream cells which are directly connected to the considered cell, to initialize the *floodplain* model:

$$F_{riv}(\mathrm{Li})_F(0) = \sum_{upstream} F_{riv}(\mathrm{Li})_{out}$$

$$\delta^7_{riv}\mathrm{Li}_F(0) = \sum_{upstream} \delta^7_{riv}\mathrm{Li}_{out} \cdot F_{riv}(\mathrm{Li})_{out} \;/\; F_{riv}(\mathrm{Li})_F(0)$$

$$Q_F = \sum_{upstream} Q_{out} + q \cdot A_{flood}$$

out stands for "leaving the cell". $\delta^7_{riv}\mathrm{Li}_F(0)$ and $F_{riv}(\mathrm{Li})_F(0)$ are the initial value of the *floodplain* model $\delta^7_{riv}\mathrm{Li}$ and $F_{riv}(\mathrm{Li})$. q denotes here the runoff and Q is the water discharge. The discharge within the considered cell floodplain (Q_F) is the sum of the discharges coming from the upstream cells plus the runoff generated by rainfall on the inundated part of the considered cell: $q \cdot A_{flood}$.

3. Integrating the *floodplain* variables $F_{riv}(\mathrm{Li})_F$ and $\delta^7_{riv}\mathrm{Li}_F$ (Eq. 7 and 10) from $x = 0$ to $x = L$.

We assumed that the integration length is equal to the square root of the cell area ($L = \sqrt{A_{cell}}$). As mentioned in the main text, the precise value of L does not matter, as long as $w \cdot L = A_{flood}$.

Equation 7 ($F_{riv}(\mathrm{Li})_F$) is solved using the 4th-order Runge-Kutta method. Q_F, w and $F_{diss}(\mathrm{Li})_F$ being constant in a cell, the equation is then a non-linear differential equation with (locally) constant coefficients.

Equation 10 is solved analytically with the approximation that $F_{riv}(x)$ and $F_{sp}(x)$ are constant between 0 and L. Regarding F_{sp} we consider $F_{sp} = \frac{1}{w}\frac{dF_{riv}}{dx} - F_{diss}$ where $\frac{dF_{riv}}{dx}$ is computed with the Runge-Kutta 4th-order method. Regarding F_{riv}, if $F_{riv}(0)$ is null, we take the value $F_{riv}(L)$, otherwise the harmonic mean between $F_{riv}(0)$ and $F_{riv}(L)$ (because Eq. 10 is divided by F_{riv}):

$$\overline{F_{riv}} = \begin{cases} F_{riv}(L) & \text{if } F_{riv}(0) = 0 \\ 2/(1/F_{riv}(0) + 1/F_{riv}(L)) & \text{otherwise} \end{cases}$$

Equation 10 becomes:

$$\frac{d\delta^7_{riv}}{dx} = -\frac{wF_{diss}}{\overline{F_{riv}}}\delta^7_{riv} + \frac{w\left(F_{diss}\delta^7_{rock} + F_{sp}\Delta_{land}\right)}{\overline{F_{riv}}} := a\delta^7_{riv} + b$$

And the analytical solution is:

$$\delta^7_{riv}(L) = \begin{cases} \left(\delta^7_{riv}(0) - b/a\right)\mathrm{e}^{-\mathrm{aL}} + b/a & \text{if } a > 0 \\ \delta^7_{riv}(0) + bL & \text{if } a = 0 \end{cases}$$

4. Mixing *hillslope* and *floodplain* outputs to compute the values leaving the cell.

At this step we define the *out* values, ie: value "leaving" the current cell towards the downstream cell. They are the result of the mixing of *hillslope* and *floodplain* output within the current cell:

$$F_{riv}(\mathrm{Li})_{out} = F_{riv}(\mathrm{Li})_H + F_{riv}(\mathrm{Li})_F(L)$$

$$\delta^7_{riv}\mathrm{Li}_{out} = \left(\delta^7_{riv}\mathrm{Li}_H \cdot F_{riv}(\mathrm{Li})_H + \delta^7_{riv}\mathrm{Li}_F(0) \cdot F_{riv}(\mathrm{Li})_F(L)\right) / F_{riv}(\mathrm{Li})_{out}$$

$$Q_{out} = \left(A_{cell} - A_{flood}\right)q + Q_F$$

Appendix D: Parameter exploration and the model optimizations.

One of the key processes of the model is the calculation of the lithium flux being removed from the water by secondary phase precipitation $F_{sp}(\mathrm{Li})$. In the absence of firm constraints, two mathematical expressions are tested (Eq. 8 and Eq. 9). Each equation has two parameters for which we tested a large range of values. For each tested combination of the two parameters, we ran the complete lithium model and assessed the modelled $\delta^7_{riv}\mathrm{Li}$ with respect to the data by computing the coefficient of determination:

$$r^2 = 1 - \frac{\sum[\Delta\delta^7_{model} - \Delta\delta^7_{data}]^2}{\sum\left[\Delta\delta^7_{data} - \overline{\Delta\delta^7_{data}}\right]^2}$$

Where $\Delta\delta^7_{data}$ stands for "measured $\delta^7_{riv}\mathrm{Li}$ minus estimated $\delta^7\mathrm{Li}$ of source rock" and $\Delta\delta^7_{model}$ for "modelled $\delta^7_{riv}\mathrm{Li}$ at the corresponding location minus $\delta^7_{rock}\mathrm{Li}$". In the model, $\delta^7_{rock}\mathrm{Li}$ is uniform and set to 1.7‰. $\overline{\Delta\delta^7_{data}}$ is the unweighted arithmetic average of $\Delta\delta^7_{data}$.

When using Eq. 8 to compute $F_{sp}(\mathrm{Li})$, the value of k_{sp} depends strongly on the value of the exponent a. Indeed, as $[\mathrm{Li}]_{riv}$ is lower than 1, k_{sp} should increase exponentially with a to maintain a "realistic" value of $k_{sp}[\mathrm{Li}]_{riv}{}^a$. This appears clearly on Fig. D1a–c showing the r^2 as a function of k_{sp} and a. For this reason, we did not explore the whole space of parameter: the white regions in Fig. D1a–c correspond to combinations of k_{sp} and a that have not been tested. Hence, the parameter optimization can be grasped looking at a only, as on Fig. D2a showing for a given a the maximum r^2 for all values of k_{sp}.

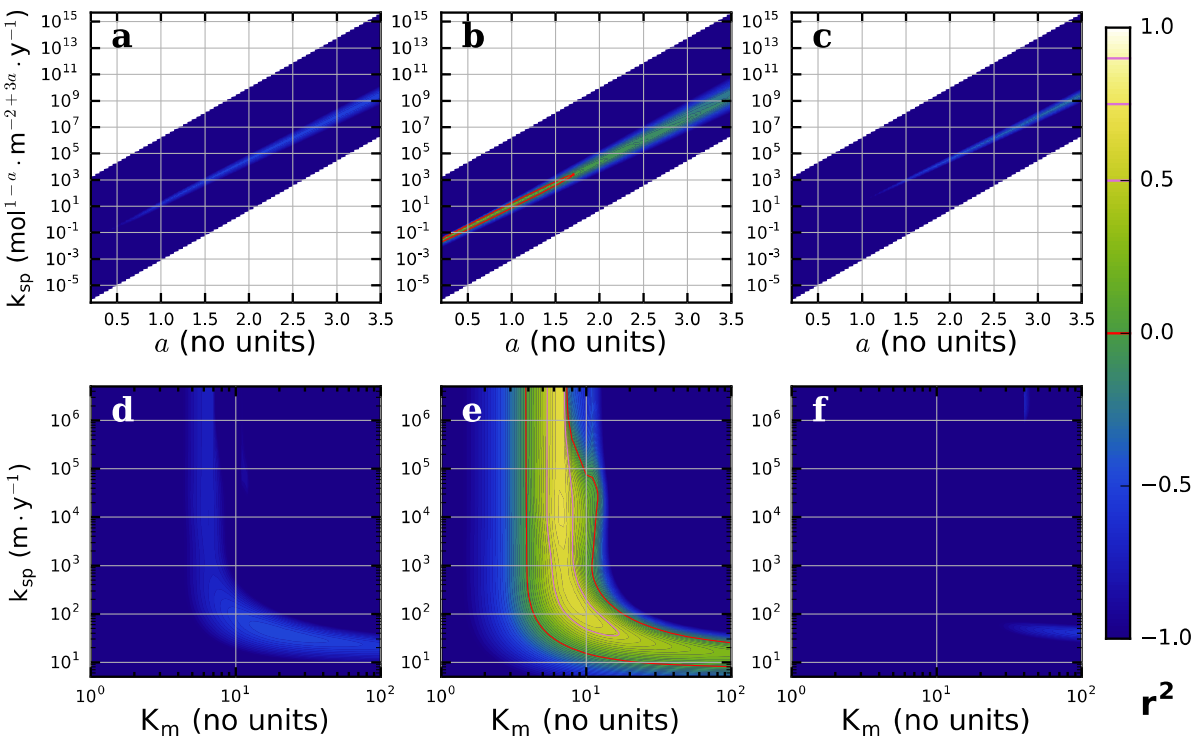

Fig. D1: Exploration of the parameters of Eq. 8 (a–c) (case #1) and Eq. 9 (d–f). (case #2). Each panel shows the data-model coefficient of determination (r^2) as a function of the two parameters: k_{sp} and a (a–c) and k_{sp} and K_m (d–f). We remind than a is equivalent to a reaction order, K_m is the saturating SP/diss ratio and k_{sp} is the kinetics constant in both equations. r^2 is computed using: (a and d) all stations (resp. case #1 and case #2); (b and e) The Madeira stations (resp. case #1-M and case #2-M); (c and f) The Solimões stations (resp. case #1-S and case #2-S).

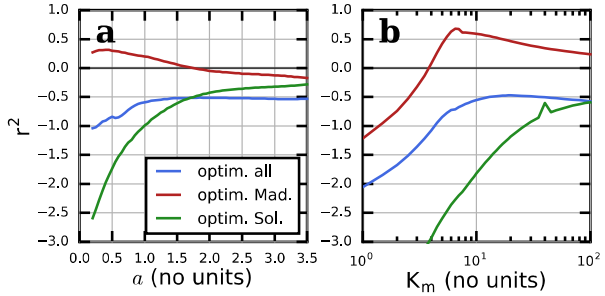

Fig. D2: Parameter exploration of Eq. 8 (a–c) or Eq. 9 (d–f). Each panel show the data-model coefficient of determination (r^2) as a function of a (a) and K_m (b). For each given value of (or K_m) the k_{sp} leading to the best r^2 has been chosen, and this best r^2 is shown on the y axis. Colour code indicates the stations that have been selected to compute the r^2.

When using the whole dataset (case #1, blue curve on Fig. D2a), the best r^2 is found for $a = 1.5$, and for higher a, it stays almost at the same value. When using only the Madeira stations (case #1-M, red curve on Fig. D2a), the best fit is for low a (0.4). When using only the Solimões stations (case #1-S, green curve on Fig. D2a), the result of the optimization is worse than with the whole dataset. r^2 reaches a plateau for a above 2.

Eq. 9 is slightly more complex to interpret. Fig. D1d–f shows the r^2 as a function of k_{sp} and K_m. The model displays two regimes depending on the value of K_m. For low K_m, F_{sp} is strongly limited by F_{diss}, and weakly by $[\mathrm{Li}]_{riv}$. This means that $\delta^7_{riv}\mathrm{Li}$ —and consequently r^2— are almost independent on the value of k_{sp}. Conversely, for high K_m, F_{sp} becomes limited by $[\mathrm{Li}]_{riv}$ and not by F_{diss}, which means that the r^2 depends on k_{sp} but very weakly on K_m. In this regime, Eq. 9 becomes equivalent to Eq. 8 with $a = 1$. Fig. D2b shows for a given K_m the maximum r^2 of all values of k_{sp}.

When using the whole dataset (case #2, Fig. D1d and blue curve on Fig. D2b), there is a plateau for intermediate values of K_m (between 10 and 50) where the maximum r^2 is found. This corresponds roughly to the transition between the two regimes. When using only the Madeira stations (case #2-M, Fig. D1e and red curve on Fig. D2b), the best regression is clearly for low K_m (between 5 and 6), in the first regime. When using only the Solimões stations (case #2-S, Fig. D1f and green curve on Fig. D2b), r^2 increases continuously within the tested range of K_m, so it is not possible to strictly define a best regression.

A last optimization has been conducted where we minimize the misfits of only the three "main" outliers of the Solimões system: the Huallaga, the Marañón at Borja and the Morona. Optimizing 2 parameters with 3 data points does not really make sense, this should rather be seen as a test of the model limits: is there a range of parameter able to produce the high $\delta^7\mathrm{Li}$ observed in these 3 rivers despite their very short path in inundated area? Only the case with Eq. 8 is discussed here. There is actually a narrow range of a (between 0.2 and 0.4) for which the r^2 computed with this 3 points is positive (Fig. D3b). Such low a leads to high and narrow "peaks of $\delta^7\mathrm{Li}$" along river paths (see Fig. B1). In addition, is also requires a kinetics constant k_{sp} around 50 to 100 times higher than for the other optimizations (Fig. D3a). Besides, Eq. 9 —that cannot generates such high and narrow peaks— never produces positive r^2 for those 3 points (not shown). Finally, the parameters best explaining these 3 rivers generate unrealistic values for almost all the other rivers (Fig. D3c).

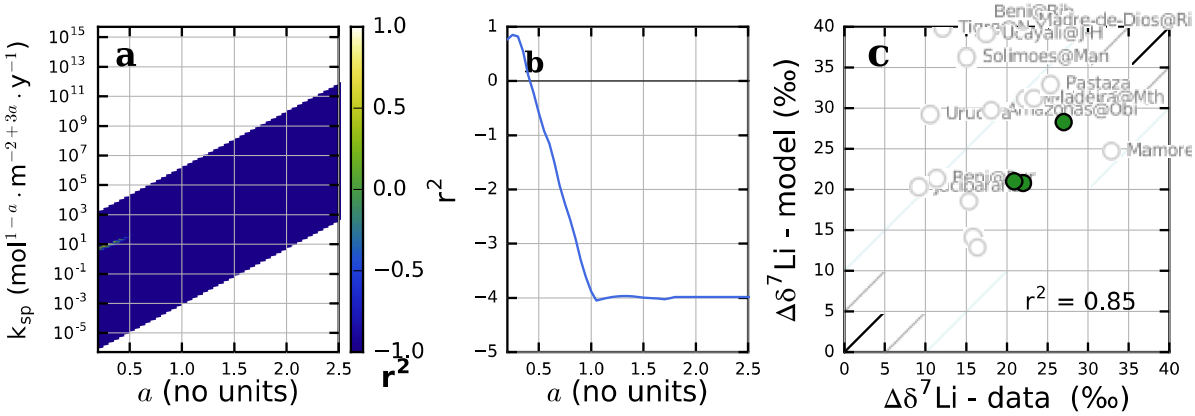

Fig. D3: Parameter exploration of Eq. 8 and optimization (according to r^2) on only three Solimões tributaries: Huallaga, Marañón at Borja and Morona. (a) same as Fig. D1. (b) same as Fig. D2 (c) same as Fig. 8.